Journal of
Marine Science and Engineering

MDPI

Article

Intercomparison of Surface Currents Obtained Using SCHISM and the HF Radar Data in Galveston Bay and Sabine Lake, Texas

Cletus O. Ogbodo [1], Rosa M. Fitzgerald [2,*], Christopher Fuller [3], Jungwoo Lee [4], Roberto Perea [2] and Javier Polanco-Gonzalez [5]

[1] Department of Environmental Science and Engineering, The University of Texas at El Paso, 500 West University Avenue, El Paso, TX 79968, USA; coogbodo@miners.utep.edu
[2] Department of Physics, The University of Texas at El Paso, 500 West University Avenue, El Paso, TX 79968, USA; raperea@gmail.com
[3] Research, Applied Technology Education Services, Inc., P.O. Box 697, Edinburg, TX 78540, USA; cfuller@office.ratesresearch.org
[4] Department of Engineering, College of Engineering and Technology, Faculty of Engineering, East Carolina University, Greenville, NC 27858, USA; leejung24@ecu.edu
[5] Department of Physics and Mathematics, Universidad Autonoma de Ciudad Juarez, Ciudad Juarez 32310, Chihuahua, Mexico; javier.polanco@uacj.mx
* Correspondence: rfitzgerald@utep.edu

Abstract: This study provides a comprehensive analysis and intercomparison of surface currents, for Galveston Bay and Sabine Lake, Texas, obtained from High-Frequency (HF) radars and SCHISM model. We established a methodology based on qualitative and quantitative analyses to compare measured and modeled surface currents. One-month HF radar data, in April 2023, were extracted from the two newly installed HF radar networks comprising two and three HF radar stations at Sabine Lake and Galveston Bay, respectively. The extracted surface current data were compared to corresponding SCHISM-simulated currents to assess the model's performance in predicting currents. The comparison encompassed qualitative and quantitative assessments by evaluating current vectors and the magnitude of eastward and northward velocity components from both methods. The results showed the ocean current predictive capabilities of SCHISM exemplified by their strong correlations (up to 0.94), high index of agreement (up to 0.95), and low error metrics, during the study period. The disparities in the eastward and northward current measurements across the dates underscore the complex interplay between prevailing winds, bay-ocean interactions, and regional weather patterns. This study sheds light on the intricate dynamics of the surface currents in estuaries and nearshore lakes with the underlying efficacy of both the HF radar and SCHISM surface current determinations. The findings can contribute to advancing the understanding of coastal dynamics and determining the strategies for environmental monitoring and management.

Keywords: HF radar; SCHISM; surface currents; estuary; Galveston Bay; Sabine Lake

Citation: Ogbodo, C.O.; Fitzgerald, R.M.; Fuller, C.; Lee, J.; Perea, R.; Polanco-Gonzalez, J. Intercomparison of Surface Currents Obtained Using SCHISM and the HF Radar Data in Galveston Bay and Sabine Lake, Texas. *J. Mar. Sci. Eng.* **2024**, *12*, 1962. https://doi.org/10.3390/jmse12111962

Academic Editor: Merv Fingas

Received: 8 September 2024
Revised: 21 October 2024
Accepted: 23 October 2024
Published: 1 November 2024

1. Introduction

The state of Texas, the United States of America, has several major estuaries along its coast including Galveston Bay and Sabine Lake. Galveston Bay (GB) and Sabine Lake (SL) are among seven major estuaries along the Texas coast that support vibrant maritime and industrial sectors. These commercial activities represent real threats to the GB and SL estuarine ecosystems, for example, due to oil and other chemical spills. The bay and lake provide tremendous economic benefits to the state and are also of industrial importance to the country. These estuaries are home to major ports for the United States, including the Port of Houston, which ranks as the nation's largest port, and sixth globally in terms of foreign tonnage. The region surrounding the bay (GB) is home to over a third of the country's chemical production facilities and oil refineries, signifying its strategic importance

in industrial operations. Moreover, the estuary contributes significantly to the economy, with one-third of commercial fishing income and half of sport fishing expenditures in Texas originating from this area [1]. SL is home to the Sabine-Neches Water Way, the third-largest port in the USA in terms of tonnage, which is the busiest military off-load port in the United States and supports a vibrant petrochemical industry that produces 60% of the nation's commercial jet fuel [2]. SL supports an estimated ~100,000 jobs and represents a huge economic asset to the nation. These characteristics have highlighted the need for the operational monitoring of the bay and the lake with special interest in measuring the surface current field in the near real time, thereby providing a prepared approach to face any future environmental mishaps—oil and substance spills. Oil spill preparedness is needed for oil exploitation and shipping in general, and surface currents are the most important variable for an oil spill model for short time scales [3].

Surface current measurements provide invaluable insight into the state of the ocean, seas, lakes, estuary surfaces, and physical nearshore processes. Measurements of surface current fields are useful for applications in marine traffic information [4], and oil spill monitoring and forecasting [5], providing a benchmark for numerical circulation models through intercomparisons [6–8]. High Frequency (HF) radars are relied on to provide invaluable real-time surface current data. CODAR SeaSonde systems can be used to measure surface currents and wave parameters (significant wave height, significant wave period, and dominant directions). The surface current is primarily determined by radars using the first-order echo of waves from the ocean surface, whose wavelength is half the transmitted wavelength [6,9]. HF radar determines currents using the first-order Doppler spectrum and wave measurements using the second-order Doppler spectrum. The classical method for ocean wave measurements relies on the second-order ocean Doppler spectrum. The analysis of this Doppler spectrum can provide additional information such as wind speed and direction, ocean wave directional spectrum, and ship activity [10].

However, alternative approaches utilize the dominant first-order Bragg echo in the HF signal, which offers a larger signal-to-noise ratio and extends the spatial coverage [11]. Similarly, as significant progress has been made in the modeling of nearshore processes in recent years [12], surface currents have been derived from computational approaches as well, complementing the efforts of observational instruments.

Traditionally, HF radars have become the most reliable source of real-time surface current maps in operational oceanography. This permits the improved monitoring of the estuaries and oceans because of their ability to cover extended areas [3], providing the synoptic reconstruction of surface current fields with spatial and temporal resolutions of up to 1 km and 1 h, respectively [13]. Each HF radar measures radial velocities and the speed of surface currents either away from or towards the radar. When these two directions are subtracted, we obtain the radial velocity field from a single radar. The combination of radial velocity from multiple radar sources is usually employed to fully deduce the east–west and north–south velocity components (most times referred to as the total velocity) [14], providing a detailed representation of the total currents. The surface current representation usually arises from the interplay of many processes including wind, waves, tides, and density variation, so the surface current is usually the cumulative measurement of all the processes and their nonlinear interactions [15]. Many applications, including Panoply (free software developed by NASA's Goddard Institute for Space Studies (GISS), used for plotting scientific data in NetCDF, HDF, GRIBB formats), enable the visualization of the current vectors obtained from HF radars with a typical hourly temporal scale [15], facilitating intercomparisons with the current vectors generated from numerical models operating at the same temporal scale.

Due to the improvements in numerical methods, the modeling of nearshore processes, and advances in computers, model systems are becoming more useful for simulating the ocean and estuarine surface circulation [12,16]. A robust three-dimensional model known as the Semi-Implicit Cross-scale Hydroscience Integrated System Model (SCHISM) was

developed to simulate surface currents and water surface elevation [5,17] and it is made up of a system of modules coupled to its hydrodynamic core.

Generally, model performance can be evaluated via model-observation (HF radar) comparisons of their horizontal velocity(currents) distributions [18], either quantitatively or qualitatively or both. Commonly adopted evaluation metrics for the quantitative comparisons include the correlation coefficient, mean square error, root mean square error, mean absolute error, and index of agreement [18–21]. Chiu [5] used the correlation coefficient to verify the accuracy and show the relationship between the simulated surface currents obtained from SCHISM and monitoring data obtained from an HF radar station. Allahdadi [20] used the Willmott index of agreement (IA) for the quantification of the model skill assessment of the simulated current and water level from the 3D hydrodynamic model, Mike3 FLOW MODEL-FM versus observation. Willmott and Matsuura [22] indicated in their findings that mean absolute error (MAE) is a more natural measure of average error; therefore, intercomparisons of the average model performance error should be based on MAE.

This work was motivated by a need to assess the performance of SCHISM in surface current simulations applied to Galveston Bay (GB) and Sabine Lake (SL) in addition to providing full real-time environmental monitoring of the bay and lake. As a result, a network of three CODAR-type HF radar stations was installed in late 2022 on GB and in January 2023, a network of two CODAR-type HF radar stations was installed in SL to perform this assessment. These HF radars began collecting surface current data starting from early 2023, with the data being provided to the public by the National Center for Environmental Information (NCEI). For this study, we focused on SCHISM outputs corresponding to the available HF radar data for April 2023 in both GB and SL. The month of April 2023 data were chosen because of the need for fully calibrated, consistent data following the installation and early-stage operations of the radars—the radars in SL only started measuring current data in March 2023. In addition, we were limited by the availability of the necessary input data for the SCHISM simulation during this period. Given the computational complexity and intensity of SCHISM requiring careful preparation and the integration of multiple input parameters, this timeframe was sufficient to provide meaningful insights into the surface current dynamics in both SL and GB. Thus, the SCHISM simulation outputs, corresponding to the HF radar data for April 2023 in Galveston Bay and Sabine Lake, were compared to verify the accuracy of the model in calculating surface currents. This work presents our retrieval of the HF radar current data, the SCHISM simulations of the surface currents and the surface current intercomparisons between them. Section 2 discusses the methods, Section 3 presents the results, Section 4 discusses the results, and Section 5 gives the conclusion.

2. Methodology

2.1. Study Area

Galveston Bay (GB) and Sabine Lake (SB) are located along the northeastern part of the Texas coast, and they are connected through the Gulf Intracoastal Waterway (GIWW). Galveston Bay is a wide shallow estuary with a total surface area of 1600 km^2 and an average depth of 3 m [1,23]. Galveston Bay is connected to the open ocean via a narrow (~200 m) and relatively deep (~14 m) shipping channel, which is called the Houston Ship Channel, through the Bolivar Roads Pass at the entrance of the bay (Figure 1). Sabine Lake, which is about 23 km long and 11 km wide, having a surface area of 253 km^2, is shallow as well, but the depth varies between 3 and 6 m depending on the sedimentation and erosion. There are deeper channels within the lake, especially along the Sabine–Neches Waterway (SNWW) where the depth averages 12 m, and efforts are underway to increase the depth to 14.6 m by the U.S. Army Corps of Engineers (USACE) [2].

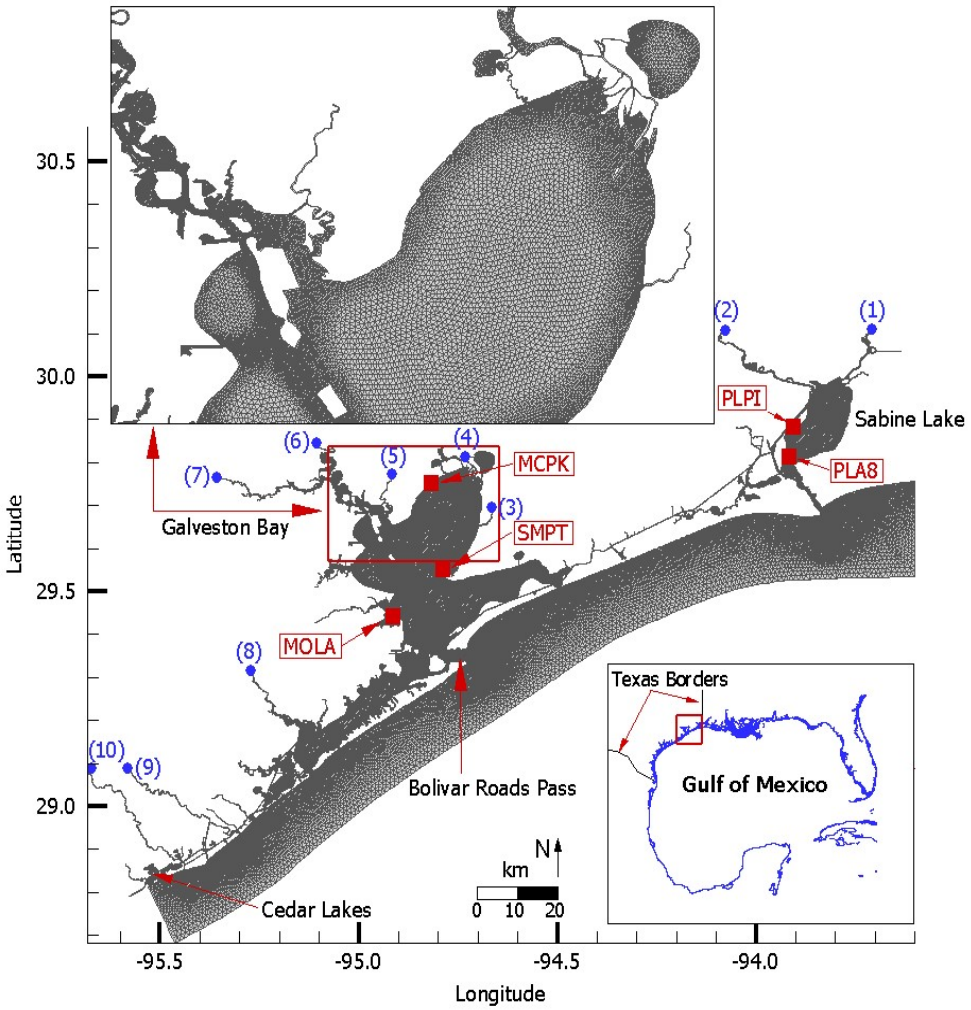

Figure 1. Map of the study area including Galveston Bay and Sabine Lake in Texas, with the model grid. The locations of the five CODAR HF radar stations in Galveston Bay (MOLA, SMPT, and MCPK) and Sabine Lake (PLPI and PLA8) are denoted by red squares. The numbers with blue dots show the river boundaries used for the SCHISM simulation.

SCHISM Setup

For the SCHISM simulation, we utilized an unstructured model grid comprising triangular and quadrilateral meshes, as outlined by [24], which also provides a comprehensive explanation of the model grid development process. The model grid extended from Cedar Lakes to Sabine Lake, encompassing approximately one-third of the Texas coast (Figure 1). The rectilinear grid was used at most ship channels, and the remaining zones were covered with triangular meshes. The final horizontal model grid consisted of 126,474 nodes and 210,510 elements with minimum and maximum grid sizes of approximately 10 m and 3000 m, respectively.

A SCHISM (version 5.8.0) was developed for the month of April 2023. The tidal offshore boundary was forced by the observed NOAA tide station data, Galveston Bay Entrance (NOAA 8771341), and Sabine Pass (NOAA 8770822) available at NOAA Tides and Currents (https://tidesandcurrents.noaa.gov; accessed on 11 August 2023). The freshwater inflows to the model domain were included at ten specified locations (ten blue dots in Figure 1; the detailed river discharge station names can be found in Table 2 by [24]) using the United States Geological Survey (USGS) gaging station data which can be accessed through the USGS National Water Information System (NWIS) (https://waterdata.usgs.gov/nwis; accessed on 11 August 2023). Finally, the North American Mesoscale forecast system (NAM) 6-hourly reanalysis data were utilized to calculate the

wind stress at each model grid available at the National Center for Environmental Prediction (NCEP) (https://www.ncdc.noaa.gov/data-access/model-data/model-datasets/north-american-mesoscale-forecast-system-nam; accessed on 11 August 2023). The simulation took place on the High-Performance Computing (HPC) facility cluster at the University of Texas at El Paso (UTEP), Jakar, in conjunction with the local workstation at the Atmospheric Physics Research laboratory at UTEP. Hourly horizontal current data were extracted from the final model simulation results for comparison with the results from the HF radar.

2.2. HF Radar

2.2.1. Network Description

To provide continuous estuarine surface currents at Galveston Bay and Sabine Lake, three Coastal Ocean Dynamics Applications Radar (CODAR)-based HF radars (also referred to as the SeaSonde HF Radar System) were installed at Galveston Bay in December 2022: (1) McCollum Park (MCPK), (2) Smith Point (SMPT), and (3) Moses Lake Tide Gate (MOLA) (Figure 1). The three installed HF radars could cover the important navigational channels in the bay including the Houston Ship Channel and GIWW [25]. The nominal operating frequency for each of the three radars was 25 megahertz (MHz), and they were determined to have a range of 30–50 km based on the inverse relation between the range of HF radar coverage and the frequency of the radar. The exact coordinates of the three radar antennae and their distances from the water are summarized in Table 1.

Table 1. Summary of the coordinates of the radars' antennae and distance from the water at Galveston Bay.

Stations Name	Latitude	Longitude	Distance from Bay
McCollum Park (MCPK)	29.744541° N	−94.828675° E	<150 m
Smith Point (SMPT)	29.546765° N	−94.788082° E	<150 m
Moses Lake Tide Gate (MOLA)	29.445450° N	−94.917287° E	<150 m

Similarly, two CODAR radars were installed in Sabine Lake with an operational frequency of 45 MHz (wavelength = 7 m), which is suitable enough to provide 10 km of coverage in the lake. The precise locations of the radars were at PLPI and PLA8 with the coordinates as shown in Table 2 below:

Table 2. Summary of the coordinates of the radars' antennae at Sabine Lake.

Station Name	Latitude	Longitude
PLPI	29.865056° N	−93.923867° E
PLA8	29.795805° N	−93.934522° E

2.2.2. HF Radar Data Source and Analysis

The radial currents from each of the HF radar networks at Galveston Bay and Sabine Lake were resolved into total vectors by the Gulf Coast Ocean Observing System (GCOOS) and incorporated into the NOAA NCEI/NDBC platform for public access. The total velocities for both eastward (u) and northward (v) water currents at Galveston Bay, Texas, and Sabine Lake were subsequently accessed from the NOAA NCEI/NDBC, and relevant software including Panoply (version 5.2.3) and Python (version 3.9.13) were utilized to analyze the data. A summary of the parameters describing the region where the dataset covered is shown in Table 3 below:

Table 3. Parameters of total vector velocities, derived from HF radar stations.

Parameters	Description
Regional Description	United States, East and Gulf Coast
Data Source	(https://www.ncei.noaa.gov/data/oceans/ndbc/hfradar/rtv/2023/202304/USEGC/; accessed on 28 August 2023)
Date Range	1 April 2023 to 30 April 2023
Latitude Range (USEGC)	21.73596° N to 46.49442° N
Longitude Range (USEGC)	−97.88385° E to −57.23121° E
Focused Study Area	Galveston Bay and Sabine Lake
Latitude Range (Galveston Bay)	29.38° N–29.78° N
Longitude Range (Galveston Bay)	−95.20° E to −94.77° E
Latitude Range (Sabine Lake)	29.55° N to 30.15° N
Longitude Range (Sabine Lake)	−94.35° E to −93.68° E
Grid Resolution	6 km

2.2.3. Data Preprocessing of the HF Radar Output

The HF radar NETCDF (Network Common Data Form) output containing both U- and V-components of the current data representing east-to-west, and north-to-south velocities was stored as 3D masked arrays where some data points were marked as invalid due to missing or corrupted measurements. A systematic filtering process was employed to remove all the missing or invalid data in Python NumPy (version 1.24.3) using a bitwise operation that allows the isolation and retention of only valid data points. The resulting clean dataset for the U- and V-components was then stored as a 1D array containing only the reliable data, ensuring the integrity of the data used to perform the intercomparisons within the study areas.

2.3. Overview of the Methods of Comparison

We established a methodology to compare the surface currents predicted by the numerical model, SCHISM, with those produced by the (HF) radar. This comprehensive evaluation encompassed both quantitative and qualitative analyses.

2.3.1. Qualitative Comparison

For the qualitative assessment, we utilized the current vector plots derived from the SCHISM outputs alongside the current vector plots obtained from the HF radar data. To facilitate this comparative examination, we examined and compared the current vectors from the HF radar data and SCHISM at identical times on the selected days. Three days are presented in the next section to provide an overall overview of the performance of both the model and the radar in generating surface currents in the bay and lake.

2.3.2. Quantitative Comparison

In a parallel effort, the quantitative aspect of our comparison entailed evaluating the magnitudes of both the eastward (u) and northward (v) velocities following [26,27]. We chose to characterize the currents in this study using the eastward (U) and northward (V) velocity components based on the available data structure from both the HF radar and the SCHISM outputs. HF radar measures currents in terms of the U- and V-components, which are common representations in oceanographic studies and are widely used in analyzing surface current patterns. On the other hand, SCHISM produces horizontal velocities, which we post-processed using Python scripts to decompose the velocities into U- and V-components. This approach ensured consistency between the two datasets (radar vs. modeled) allowing for a direct comparison of the two. Decomposing the SCHISM horizontal velocity variable into the U- and V-components allowed us to capture the primary directional flow and align it with the available radar data, while maintaining the accuracy and consistency of our analysis. To distinguish each current vector component derived by using each method, we use the following naming approach throughout this paper: *Uschism* and *Vschism* for

the SCHISM data, and *U_HFR_6* and *V_HFR_6* for the HF radar data, for the eastward and northward component, respectively. The "6" added to U_HFR and V_HFR is used to indicate the resolution (6 km) of the radars used for this analysis.

A SCHISM was set up to generate an output every 1 h. The sampling frequency of our radars was 0.1 Hz (1 sample every 10 min). This means that radial HF radar velocities were generated at each remote SeaSonde station (McCollum Park (MCPK), Smith Point (SMPT), Moses Lake Tide Gate (MOLA), PLPI, and PLA8) from 15 min cross spectra output with an output rate of one cross spectrum file every 10 min (creating an overlap). Note that the lower output rate with respect to the cross spectra averaged time indicates that there was some overlap in the cross spectra averaging (improving the continuity and accuracy of the current velocity measurements). Radial vectors were then generated hourly from a total of seven cross spectra files, representing a coverage time of 75 min. Radial vector files were then transferred for Real Time Vector processing by HFRnet through a cooperative effort with GCOOS, and data were served to the public via the U.S. Integrated Ocean Observing System. Hourly total resolved vectors were hence made available through the NOAA HF Radar National Server at https://hfradar.ndbc.noaa.gov/.

In our quantitative analysis, we utilized the average values of these hourly outputs for both the radar and model velocities considering the varying amounts of spatial data generated by SCHISM and the radar system. We used the following four error analysis methods: (1) correlation coefficient (*corr*), (2) root mean square error (RMSE), (3) mean absolute error (MAE), and (4) the Willmott index of agreement (IA) to evaluate the performance of our model against observations.

A correlation coefficient is a statistical measure of how one variable changes with respect to another variable. The most common measure of correlation in statistics is the linear correlation coefficient *corr* which measures the strength and direction of a linear relationship between two variables, and is determined as follows:

$$corr = \frac{N\sum xy - (\sum x)(\sum y)}{\sqrt{N\left(\sum x^2\right) - \left(\sum x\right)^2}\sqrt{N\left(\sum y^2\right) - \left(\sum y\right)^2}} \quad (1)$$

where x(simulated) and y(observation) denote the two variables and n is the total number of variables. The range of *corr* is between −1 and +1. The + and – signs indicate positive and negative linear correlations, respectively. If x and y have a strong positive linear correlation, *corr* is close to +1. A correlation greater than 0.8 is generally described as strong, whereas a correlation less than 0.5 is generally described as weak [5].

$$\mathrm{RMSE} = \sqrt{\sum_{i=1}^{N} \frac{(y_i - x_i)^2}{N}} \quad (2)$$

is a measure of the differences between the simulated (x_i) and observed y_i values, with lower values (closer to zero) indicating a better relationship between the observed and simulated values, and N is the total number of variables [19].

MAE measures the magnitude of the average deviation between the model value (x_i) and observation value (y_i) [28].

$$\mathrm{MAE} = \frac{\sum_{i=1}^{N} |x_i - y_i|}{N} \quad (3)$$

The index of agreement (IA) proposed by [21] was used for a quantitative comparison of the model performance in the simulation of currents in the bay and lake. The index of agreement is given as:

$$\mathrm{IA} = 1 - \frac{\sum_{i=1}^{N} (x_i - y_i)^2}{\sum_{i=1}^{N} (|x_i - \overline{y}| + |y_i - \overline{y}|)^2} \quad (4)$$

where y_i and x_i are the observed and model values, respectively; $\overline{y}$ denotes the mean values of observations. The index values vary between 0 for poor agreement and 1 for a perfect match [21,28].

3. Results

There were three outcomes observed from the results of our intercomparison analysis:

(i) days when both eastward and northward currents dominate the bay or lake.
(ii) days when mostly a northward current dominates the bay or lake.
(iii) days when mostly an eastward current dominates the bay or lake.

Consequently, in this section, we outline the outcome of the simulation and analysis concerning a representative day on which both eastward and northward currents were present as measured by the HF Radar and modeled at GB. This implies the day when both eastward and northward directed currents dominated the bay. Additionally, we present the result for a representative day when only northward directed currents dominated in the bay, and a representative day when only eastward directed currents dominated in the bay as both observed by the radar and model with a significant correlation. In the final section (Section 3.4), we also present the result from a representative day when only northward currents dominated SL. We summarize in Tables 4 and 5 the additional days when we obtained similar outcomes as described above.

Table 4. Summary statistics for model and radar performance for each of the velocity components in GB.

Date/Components	Corr.	RMSE (m/s)	MAE (m/s)	IA
6 April				
U-component	0.63	0.1	0.09	0.47
V-component	0.32	0.1	0.09	0.44
7 April				
U-component	0.63	0.07	0.06	0.68
V-component	0.12	0.08	0.07	0.41
8 April				
U-component	0.94	0.02	0.02	0.95
V-component	0.76	0.04	0.03	0.83
9 April				
U-component	0.86	0.04	0.03	0.88
V-component	0.58	0.06	0.05	0.6
10 April				
U-component	0.38	0.06	0.05	0.58
V-component	0.55	0.07	0.07	0.42
11 April				
U-component	0.11	0.11	0.1	0.33
V-component	0.66	0.08	0.07	0.64
12 April				
U-component	0.52	0.15	0.13	0.28
V-component	0.78	0.08	0.07	0.68
13 April				
V-component	0.17	0.1	0.09	0.26
14 April				
U-component	0.1	0.1	0.08	0.38
V-component	0.35	0.07	0.06	0.45
15 April				
V-component	0.55	0.09	0.06	0.56
16 April				
U-component	0.51	0.07	0.06	0.52
V-component	0.51	0.08	0.07	0.52
17 April				

Table 4. *Cont.*

Date/Components	Corr.	RMSE (m/s)	MAE (m/s)	IA
U-component	0.38	0.05	0.04	0.54
V-component	0.79	0.07	0.06	0.52
18 April				
U-component	0.65	0.1	0.1	0.27
V-component	0.41	0.07	0.07	0.62
19 April				
U-component	0.89	0.04	0.03	0.85
V-component	0.59	0.05	0.04	0.76
20 April				
U-component	0.27	0.07	0.05	0.41
21 April				
U-component	0.64	0.06	0.05	0.76
V-component	0.24	0.09	0.07	0.48
22 April				
U-component	0.26	0.07	0.07	0.47
V-component	0.08	0.09	0.08	0.36
23 April				
U-component	0.11	0.07	0.06	0.41
V-component	0	0.09	0.08	0.35
24 April				
U-component	0.87	0.04	0.03	0.85
V-component	0.21	0.11	0.09	0.39
25 April				
U-component	0.57	0.05	0.04	0.73
V-component	0.66	0.06	0.05	0.65
26 April				
U-component	0.46	0.05	0.05	0.54
V-component	0.95	0.05	0.04	0.83
27 April				
U-component	0.22	0.07	0.06	0.38
V-component	0.9	0.09	0.08	0.62
28 April				
U-component	0.39	0.06	0.05	0.4
V-component	0.92	0.09	0.09	0.53
29 April				
V-component	0.51	0.07	0.06	0.42
30 April				
U-component	0.45	0.05	0.04	0.59
V-component	0.78	0.06	0.05	0.72

Table 5. Summary statistics for model and radar performance for each of the velocity components in SL.

Date/Component	Corr.	RMSE (m/s)	MAE (m/s)	IA
7 April				
V-component	0.08	0.06	0.04	0.39
8 April				
V-component	0.3	0.04	0.05	0.44
9 April				
U-component	0.04	0.07	0.06	0.43
V-component	0.3	0.04	0.03	0.48
10 April				
U-component	0.07	0.04	0.03	0.33
12 April				
U-component	0.25	0.17	0.16	0.22
13 April				

Table 5. *Cont.*

Date/Component	Corr.	RMSE (m/s)	MAE (m/s)	IA
U-component	0.6	0.06	0.05	0.47
14 April				
V-component	0.62	0.04	0.03	0.54
15 April				
U-component	0.13	0.11	0.1	0.32
16 April				
U-component	0.15	0.06	0.05	0.4
V-component	0.24	0.06	0.05	0.4
17 April				
U-component	0.42	0.06	0.05	0.44
V-component	0.39	0.03	0.02	0.4
18 April				
V-component	0.65	0.08	0.06	0.42
19 April				
V-component	0.29	0.05	0.04	0.32
21 April				
U-component	0.51	0.07	0.06	0.5
V-component	0.55	0.06	0.05	0.49
22 April				
V-component	0.28	0.04	0.03	0.53
23 April				
U-component	0.27	0.04	0.03	0.43
24 April				
U-component	0.02	0.06	0.05	0.35
V-component	0.6	0.05	0.04	0.53
25 April				
U-component	0.76	0.04	0.03	0.48
V-component	0.52	0.03	0.03	0.48
26 April				
U-component	0.59	0.02	0.02	0.56
V-component	0.05	0.06	0.05	0.48
27 April				
U-component	0.1	0.06	0.05	0.36
V-component	0.95	0.09	0.08	0.47
28 April				
U-component	0.56	0.05	0.05	0.39
29 April				
V-component	0.01	0.07	0.06	0.34
30 April				
U-component	0.14	0.05	0.04	0.42
V-component	0.8	0.04	0.03	0.6

3.1. Northward and Eastward Currents in GB

On 8 April, it was observed that the dominant surface currents in GB had both the eastward and northward components of the currents. These are illustrated by both the qualitative and quantitative component analysis in the following sections.

3.1.1. Qualitative Comparison on 8 April at GB

In our observation, we considered northward and eastward directions as positive while currents directed southward, and westward were considered negative. Figure 2a,b shows the current vector for the entire bay from both the SCHISM and HF radar data. It was observed that there were more model vectors than observed vectors from the radars, making it harder to visually assess how the currents in both were oriented. Thus, to provide a closer view of the currents' orientation during this hour (2 p.m.), we added a subplot (Figure 2c) from a portion of the bay as generated by SCHISM for a clearer comparison with a radar plot. Also, to further enhance the comparison, the area shown in the subplot

(Figure 2c) is also shown in Figure 2a,b by the box (rectangular) with a red outline. In Figure 8b, this subplot is shown by a box with a yellow outline to distinguish it from the original color of the current vectors. In Figure 11b, the subplot is also represented by a box with a blue outline so as not to confuse it with the original color of the current vectors. This applied to all the qualitative analyses presented in this paper.

In Figure 2, the radar plot (Figure 2b) and the SCHISM bay subplot (Figure 2c) reveal the dominant directions indicated by both methods for north-westward, north-eastward, and northward. The model subplot (Figure 2c) covers a small portion of the bay, while the radar plot encompasses the entire bay (see the boundaries of the bay plotted in Figure 2b), thus displaying the current vectors in many more directions than the subplot from SCHISM.

The color bar used in Figure 2b indicates the magnitude of the water velocity, and the formula shown on the bar combines both the eastward (U) and northward (V) components into a single speed value—the speed of the surface current. The cooler color (blue) in the bar indicates lower velocities, while the yellow to red colors indicate higher velocities, thus showing the variation in the current magnitude across the plotted area. Also, the reference value indicated at the end of the color bar refers to the scale of the vector arrows. In Figure 2b, the reference value is 0.5 (which means 0.5 m/s), and the arrow above it implies that the plotted vectors (current arrows) are scaled relative to 0.5. So, an arrow (current vectors) half the length of the reference arrow would indicate a current speed of 0.25 m/s. This helps readers to understand the magnitude of the currents by visually comparing the arrow sizes. The two triangles at the end of the color bar represent the outlier borders which help to ensure that extreme values (>0.5 or <0.0) are visually distinguished from the primary data range. Finally, the plotting boundaries (latitude (29.305° N–29.805° N), longitude (−95.015° E to −94.655° E)), defining the spatial extent of the data denoting the study area (in this case GB) have been added in the plot. The above explanation applies to all the radar plots (Figures 2b, 5b, 8b, and 11b) presented in this paper.

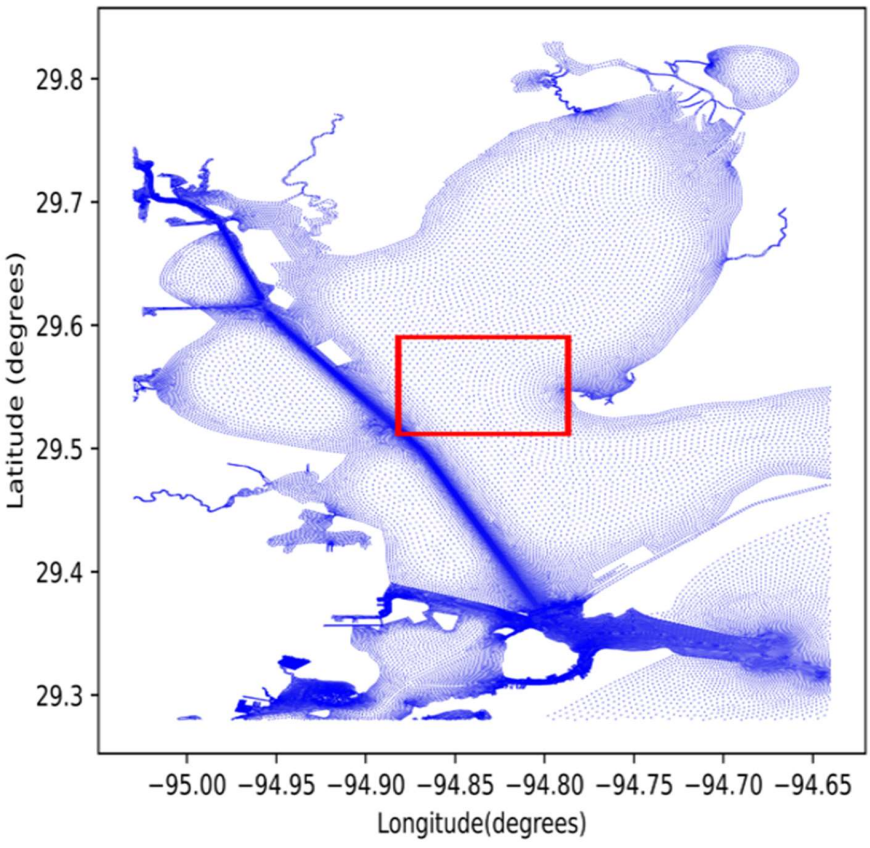

(**a**) SCHISM

Figure 2. *Cont.*

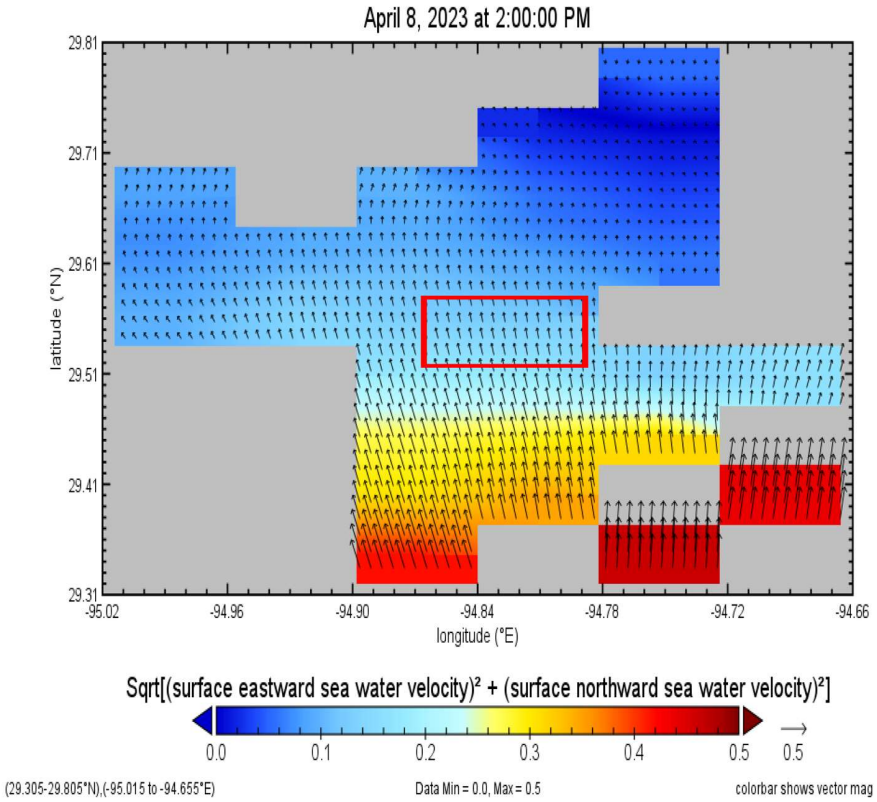

(**b**) HF radar

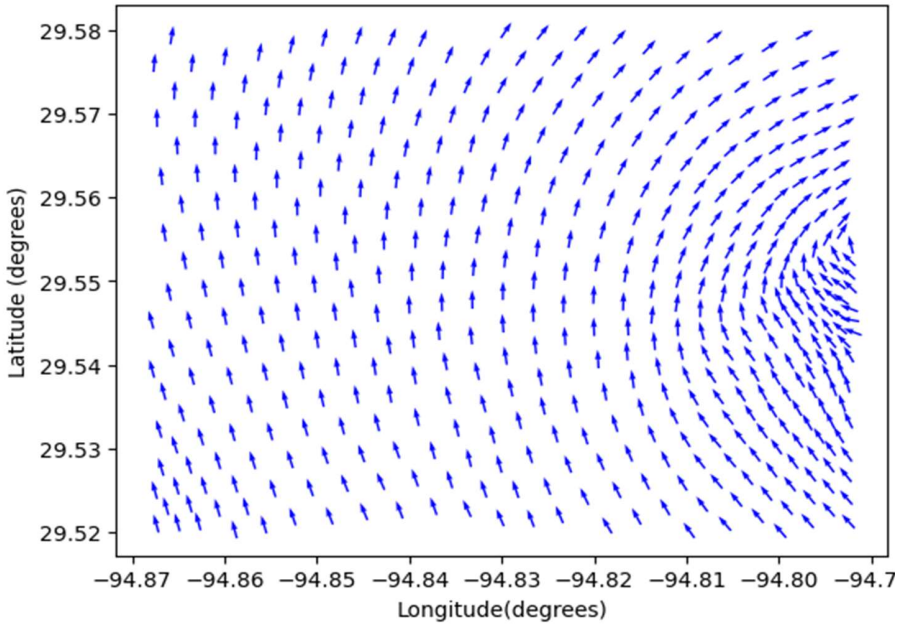

(**c**) A subplot of (**a**)

Figure 2. Plot of total current vectors produced by (**a**) SCHISM and (**b**) HF radar in GB (whole bay) at 2 p.m., 8 April 2023—color bar represents magnitude of current speed in m/s. (**c**) A subplot (from a portion of the bay denoted by red square in (**a**)) of Total Current Vectors Derived from SCHISM in Galveston Bay at 2 p.m., 8 April 2023.

3.1.2. Quantitative Comparison, 8 April at GB

In this section, we present the analysis based on 24 data points corresponding to each hour of a particular day. For each hour, we averaged the U- and V-components of the surface

across all the available radar grid points (~5000) and all the SCHISM grid points (~46,500). This means that for each hour, the average radar current magnitude (U- and V-components) was compared with the average current magnitude (U- and V-components) from SCHISM. This method of using averaged data (current radar grid points or current from the SCHISM grid points) was applied consistently for all the quantitative comparisons made on the selected days. The analysis below illustrates the comparisons derived from these averages.

Figures 3 and 4 reveal a notable congruence between SCHISM and HF radar, portraying appreciable alignment in measuring the intensity and orientation of surface currents (water velocity) on 8 April 2023, in Galveston Bay, Texas. This suggests a persistent occurrence of both eastward and northward surface water velocities in the bay throughout the day. Particularly, Figure 3a,b shows close alignment in the time series diagram of the currents produced by using both methods in the eastward and northward directions, respectively. Figure 4a,b shows the correlations between the simulated and observed total current speed (water velocity) for the eastward and northward directed water movement in that order. Figure 4a shows that there is a strong correlation coefficient of around 0.94 between the currents generated by the model and radar in the eastward (westward) direction. Figure 4b depicts that the correlation coefficient between the radar and model measurements in the northward direction was observed to be 0.76.

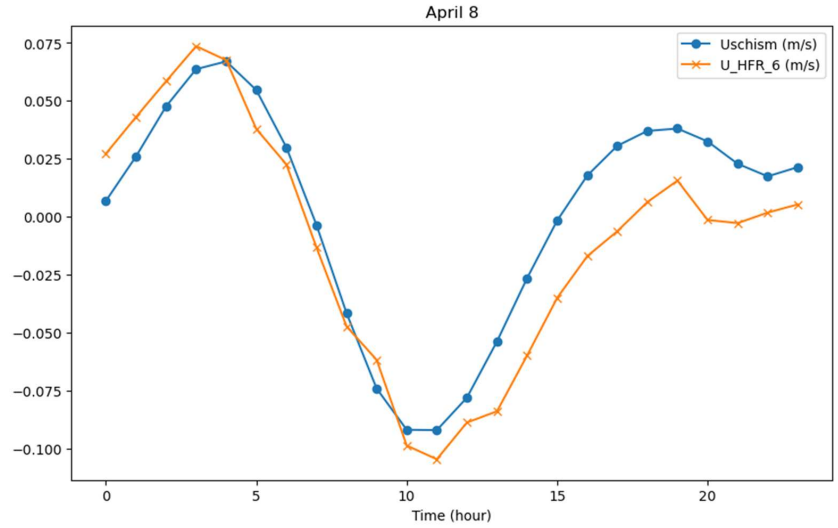

(**a**) Eastward currents

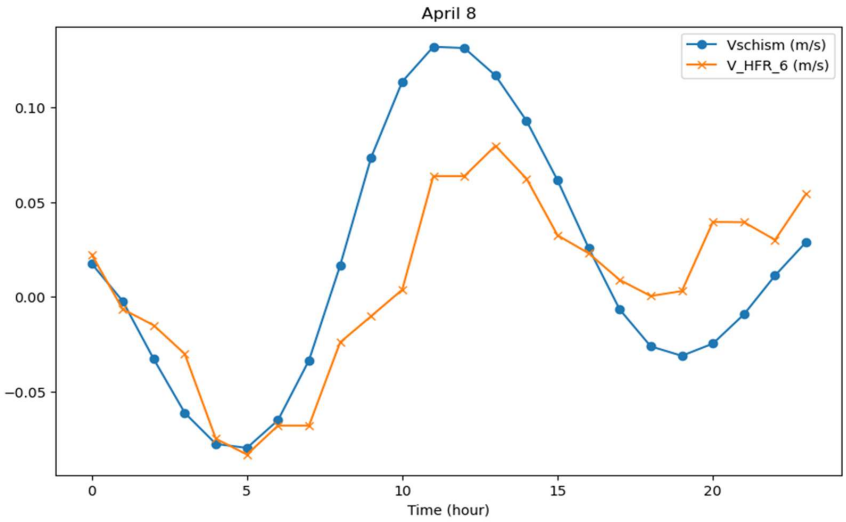

(**b**) Northward currents

Figure 3. Comparison of (**a**) eastward currents from model (Uschism) and HF radar (U_HFR_6) 8 April 2023; (**b**) northward currents from model (Vschism) and HF radar (V_HFR_6) for the entire 24 h of 8 April 2023 at Galveston Bay.

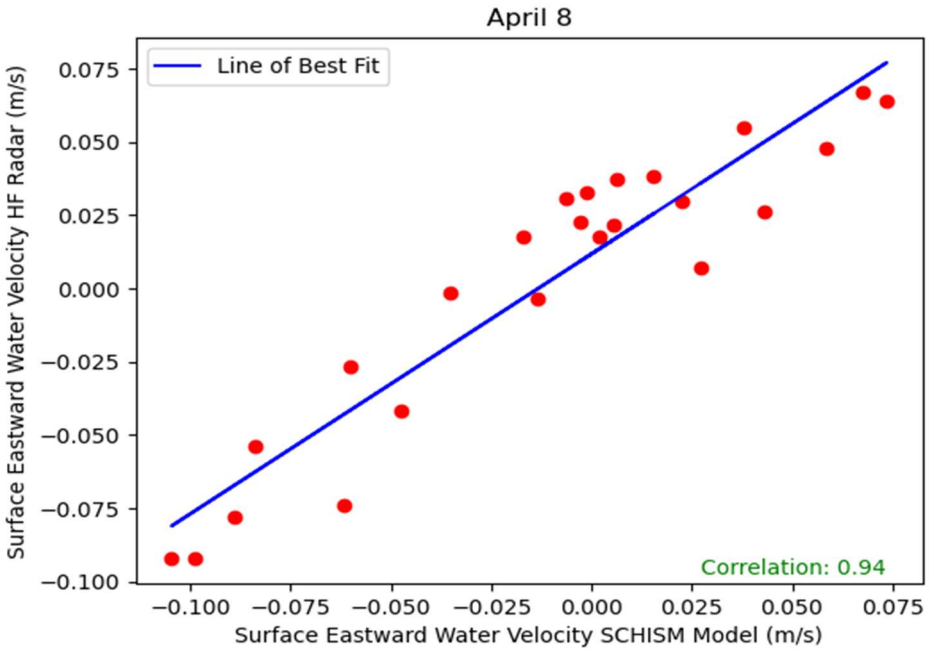

(**a**) Eastward currents

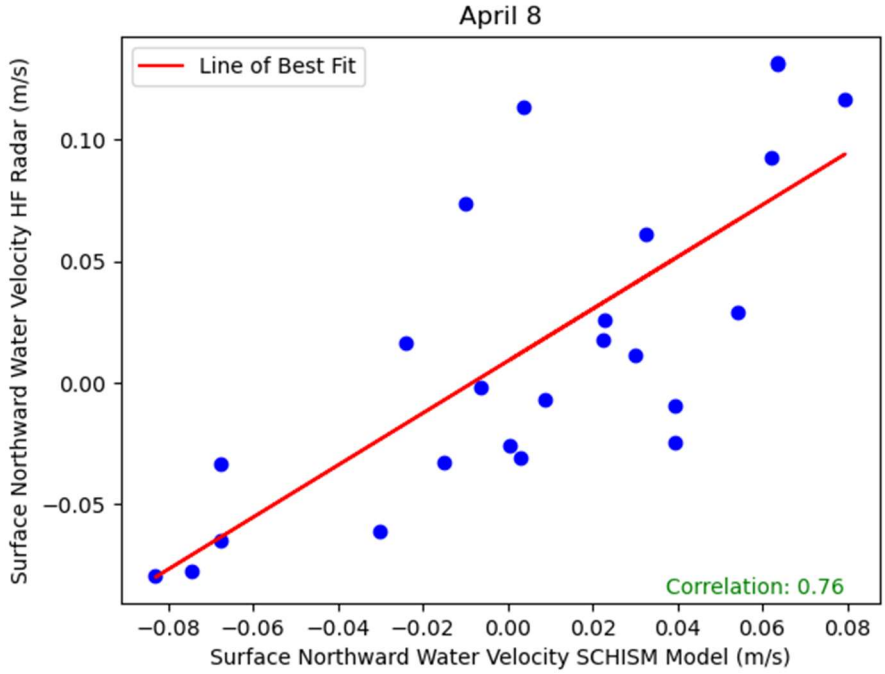

(**b**) Northward currents

Figure 4. Correlation between the simulated (SCHISM) and observed (HF radar) hourly averages of currents (total water velocity) in (**a**) eastward and (**b**) northward directions for the entire 24 h of 8 April 2023, in GB.

Upon closer examination of the qualitative analysis in Figure 2, most of the currents captured by both methods in the bay (GB) at 2 p.m. on 8 April predominantly flowed north-eastward and north-westward. Whereas the qualitative analysis represents current vectors from both the model and the radar at only one hour at 2 p.m. of the day, the quantitative comparison considered the current magnitudes throughout the 24 h of the day. It could have been that most of the currents were coming from the east into the bay and moving towards the north of the bay that day based on the observation from the quantitative analysis above which showed significantly strong correlation coefficients in the eastward currents

(0.94) and significant correlation (0.76) in the northward currents. The results suggest close tracking and measurement alignment between SCHISM and HF radar, demonstrating their ability to measure similar values in eastward surface currents at Galveston Bay on 8 April 2023. In addition, the correlation coefficient of 0.76 in the northward direction also indicates that both methods captured similar trends and magnitudes in northward water velocities on this day at GB. The other evaluation metrics as presented in Table 4 showed that the RMSE and MAE in the measurement of the eastward currents by both methods were, respectively, 0.02, while the IA between the model and radar measurements was 0.95. On the other hand, the RMSE and MAE for the northward currents were 0.04 and 0.03, respectively, while the IA between the model and radar measurements of the northward component of the currents on this day was 0.83. The high IA values and low RMSE and MAE values point to the high level of agreement between the model's and actual radar measurements of the currents on this day.

3.2. Northward Currents in GB

On 27 April, it was observed that the predominant current in the bay was mostly a northward (negative northward, i.e., moving southward) directed current. This is illustrated in the section below.

3.2.1. Qualitative Analysis on 27 April at GB

The qualitative analysis in Figure 5b,c shows that the southward (negative northward) surface currents were the dominant currents in GB at 9 a.m. on 27 April 2023. The implication of this is that the primary water movement in the bay at that time of the day was southward. This current direction and presence of less prominent eastward (and westward) currents could be a result of a combination of factors such as tide, prevailing wind patterns, or coastal geography.

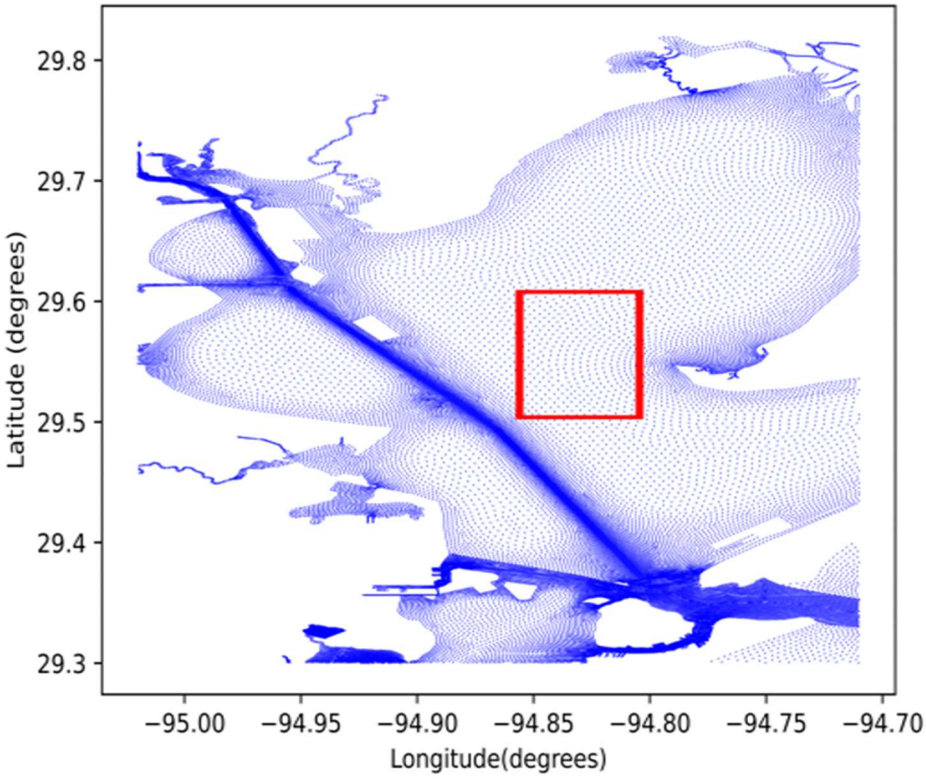

(**a**) SCHISM

Figure 5. *Cont.*

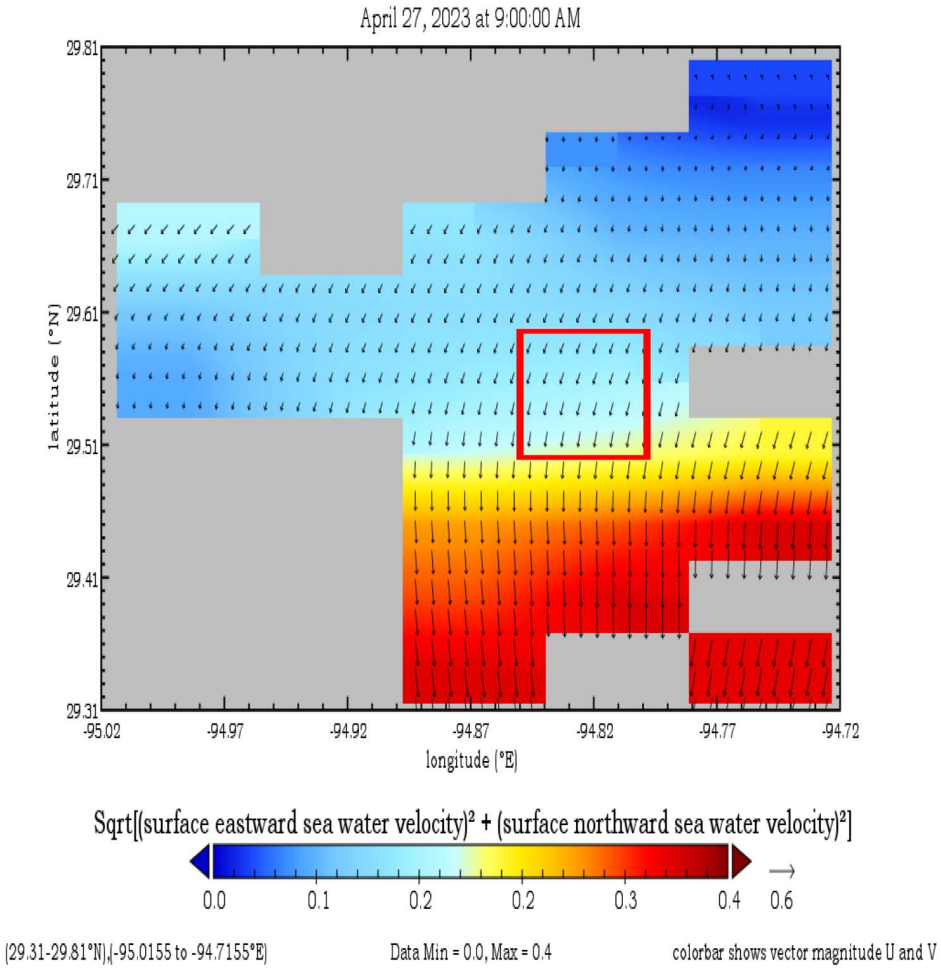

(**b**) HF radar

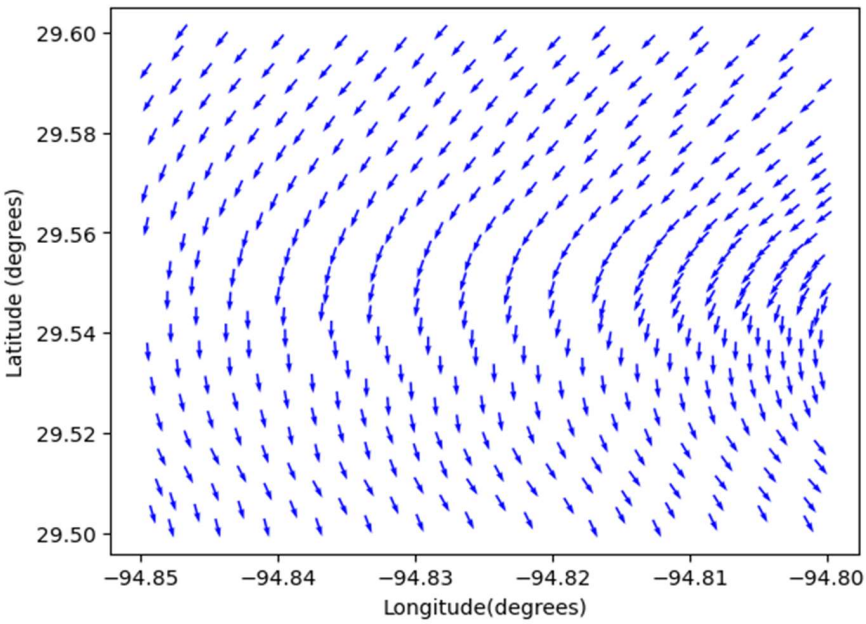

(**c**) A subplot of (**a**)

Figure 5. The plot of total current vectors produced by (**a**) SCHISM and (**b**) HF radar in GB (whole bay) at 9 a.m., 27 April 2023—color bar represents magnitude of current speed in m/s. (**c**) A subplot (from a portion of the bay denoted by red rectangle in (**a**)) of Total Current Vectors Derived from SCHISM in Galveston Bay at 9 a.m. on 27 April 2023.

3.2.2. Quantitative Comparison on 27 April at GB

From Figure 6, in the first 12 h of the day (27 April) the model underestimated the speed of the currents by more than 0.1 m/s, and even showed the currents to be in the opposite direction. Despite underestimating the speed, the model, however, represented the trend well over the entire 24 h. This observation could be due to data gaps in the radar measurements in the bay or perhaps the inability of the model to capture small-scale variations unlike the radar.

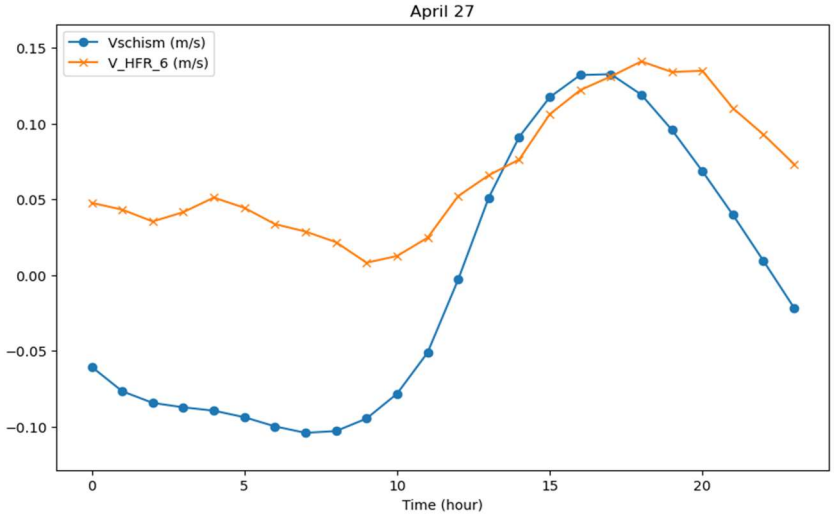

Figure 6. Comparison of northward currents from SCHISM (Vschism) and HF radar (V_HFR_6) over time at GB on 27 April 2023.

The strong significant correlation coefficient of 0.90 between the northward surface current magnitudes estimated by the model with the radar on 27 April (Figure 7) reinforces the earlier qualitative comparison (Figure 5), which showed dominant northward water movement in the bay. This suggests that days with high correlation in the northward direction indicate consistent northward flow, signifying the stable water movement pattern appreciably captured by the model and radar.

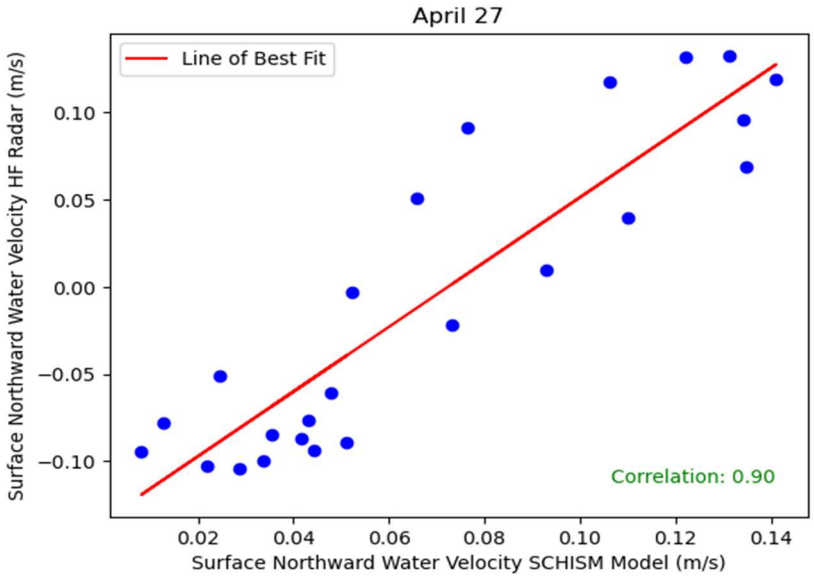

Figure 7. Correlation between the simulated (SCHISM) and observed (HF radar) hourly averages of northward currents (total water velocity) at GB for entire 24 h of 27 April 2023.

Table 4 shows that the RMSE and MAE values between the model and radar measurements on this day were estimated to be 0.09 and 0.08, respectively. The IA value between the two methods was 0.62. The error values are considered large since the small magnitude of currents typically from 0.05 to 0.1 m/s was measured by both the radar and the model. These large errors and the relatively small IA values could be attributed to the above observation in Figure 6.

3.3. Eastward Currents in GB

On 6 April, it was observed that the dominant current direction in the bay was mostly eastward (negative eastward, i.e., moving westward). We present this result in the following section.

3.3.1. Qualitative Analysis on 6 April at GB

The qualitative analysis of the current vectors shown in Figure 8 above shows that the eastward currents dominated, particularly in the negative east direction (westward, southwestward, northwestward). Both methods capture these current directions at this time of the day further suggesting their capability in effectively detecting the predominant flow patterns within the bay. Again, the subplot (Figure 8c) is derived from just a portion of the bay (−94.99° E to −94.93° E and 29.51° N to 29.56° N), whereas the radar plot (Figure 8b) represents the entire bay. The part of the bay equivalent to the subplot (Figure 8c) is shown by the box with a yellow outline.

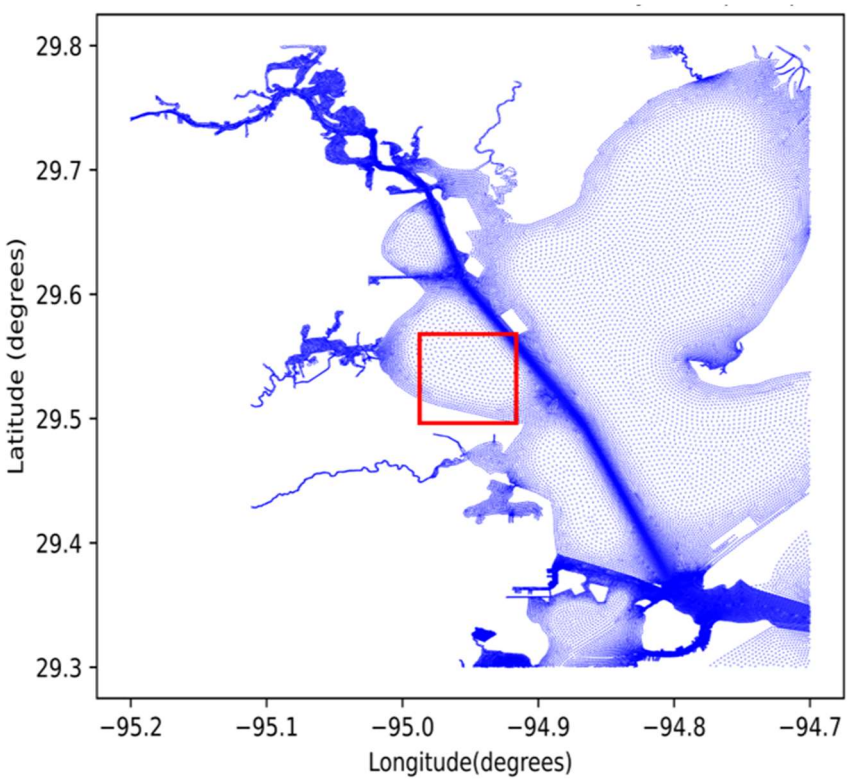

(**a**) SCHISM

Figure 8. *Cont.*

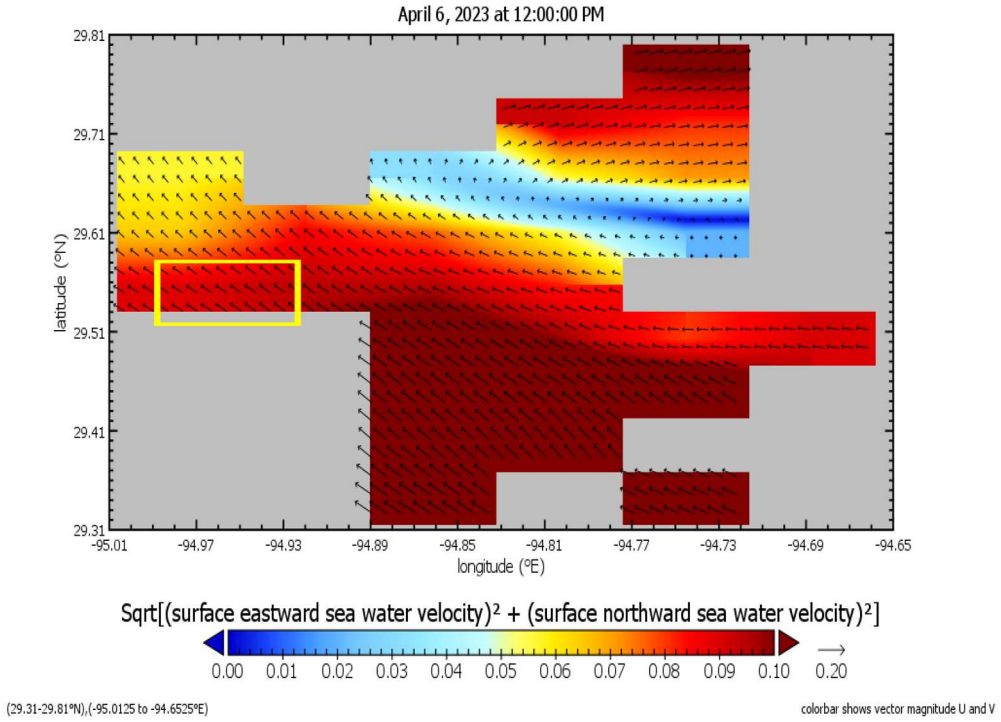

(**b**) SCHISM

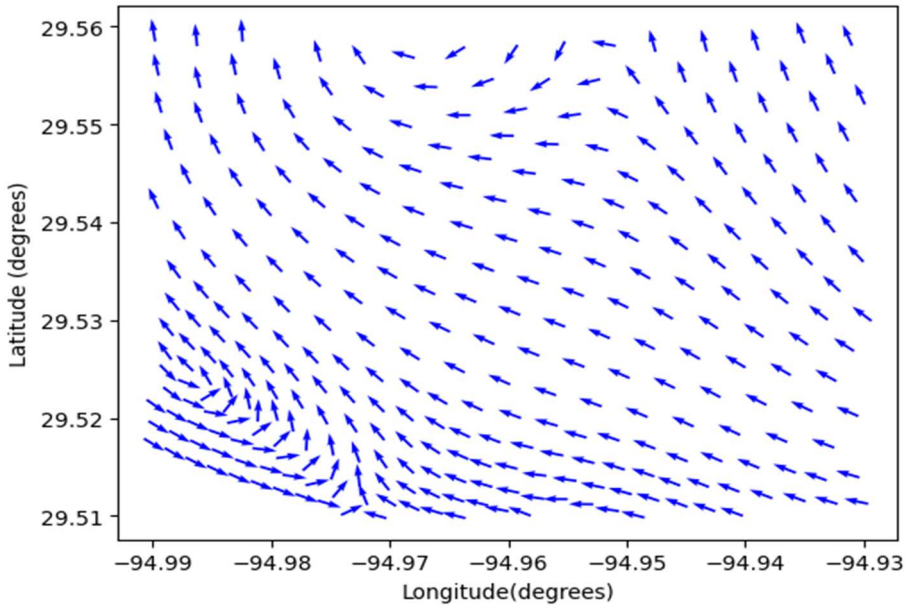

(**c**) A subplot of (**a**)

Figure 8. Plot of total current vectors produced by (**a**) SCHISM and (**b**) HF radar in GB (whole bay) at 12 p.m., 6 April 2023—color bar represents magnitude of current speed in m/s. (**c**) A subplot (from a portion of the bay denoted by the red square in (**a**)) of Total Current Vectors Derived from SCHISM Model in Galveston Bay 6 April 2023 at 12 p.m.

3.3.2. Quantitative Comparison on 6 April at GB

The more prevalent westward (north-westward, south-westward) currents evident in the qualitative analysis in Figure 8 were further confirmed by the moderate yet significant correlation coefficient in the eastward current as measured by the model and observation (Figures 9 and 10). In Figure 9, it is apparent that both the model- and radar-generated currents follow the same trajectory, suggesting their ability to track the trends in water

movement across the bay through the day despite the discrepancies in their current direction. However, it is noteworthy that the numerical values recorded by the model are smaller in magnitude than those measured by the radar. Again, the model and radar measured currents in opposite directions for most hours of the day. Consequently, this stark difference accounts probably for the observed moderate correlation of 0.63 in Figure 10. The RMSE and MAE values from Table 4 on this day as measured by both methods were 0.1 and 0.09, respectively. The IA value of 0.47 suggests that both methods were not quite in agreement with their estimation of the surface currents in the bay throughout that day.

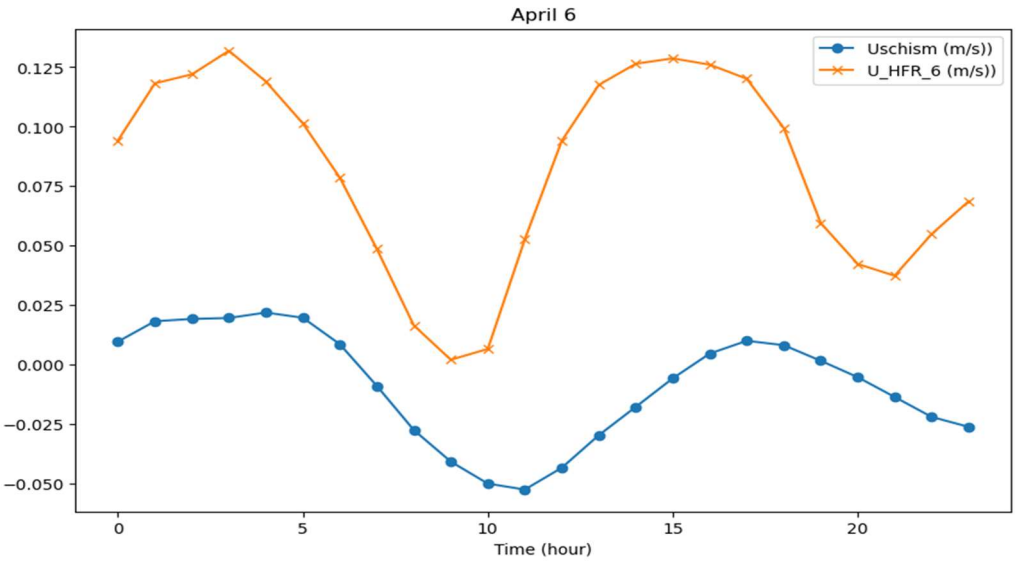

Figure 9. Comparison of eastward currents from SCHISM (Uschism) and HF radar (U_HFR_6) over time at GB on 6 April 2023.

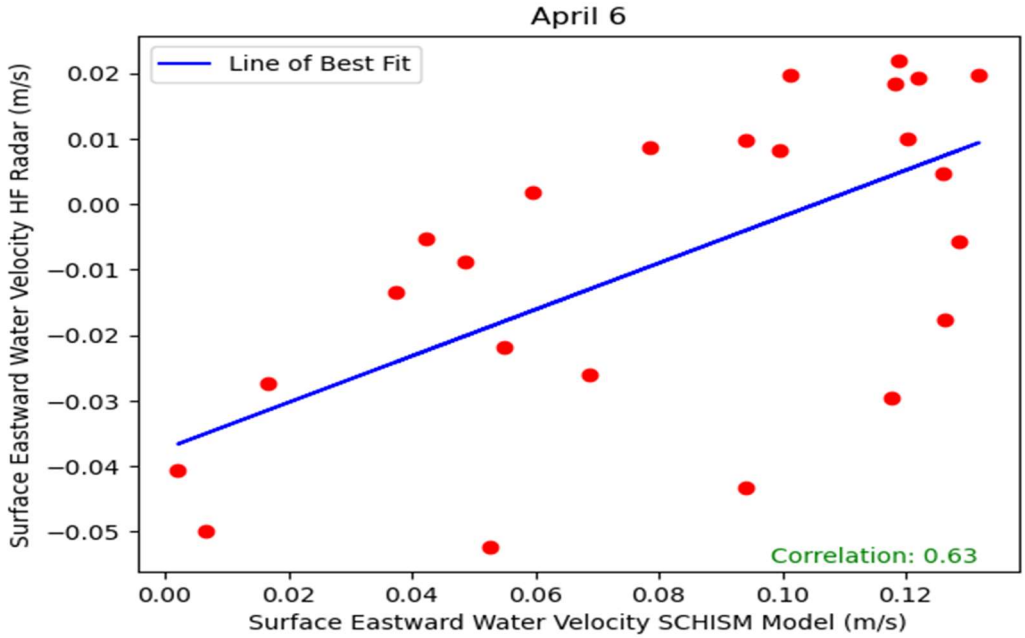

Figure 10. Correlation between the simulated (SCHISM) and observed (HF radar) hourly averages of eastward currents (total water velocity) at GB for entire 24 h of 6 April 2023.

3.4. Northward Currents in SL

On 27 April, in the lake, it was observed that the predominant current direction was mostly northward (negative northward, i.e., moving southward). So, we had more southward-directed movement of water. This is illustrated in the section below.

3.4.1. Qualitative Analysis on 27 April at Sabine Lake

The observations from Figure 11 above highlight a prevailing northward (negative northward, i.e., southward) current in Sabine Lake at 9 a.m. on 27 April. The fact that the current vectors from both the HF radar and SCHISM illustrate similar southward trends at this specific time signifies the agreement in their observations (even though their exact directions differ slightly—while the model's direction is south-westward, the radar's direction at the highlighted portion is south-southward, and south-eastward). The model subplot in Figure 11c represents only a portion of the lake (−93.89° E to −93.84° E, 29.86° N to 29.92° N) while Figure 11a represents the whole lake (−94.4° E to −93.6° E, 29.6° N to 30.1° N).

The plotted section depicted in Figure 11b represents an area where the radar had difficulty in capturing enough current vectors. The precise boundaries of the region of the lake plotted are indicated in the footnote of Figure 11b, providing clarity of the spatial extent of measurements at that time of the day. Similarly, the model subplot (Figure 11c) also reflects a comparable scarcity of current vectors in this region, further underscoring the challenges in accurately capturing the surface currents within Sabine Lake.

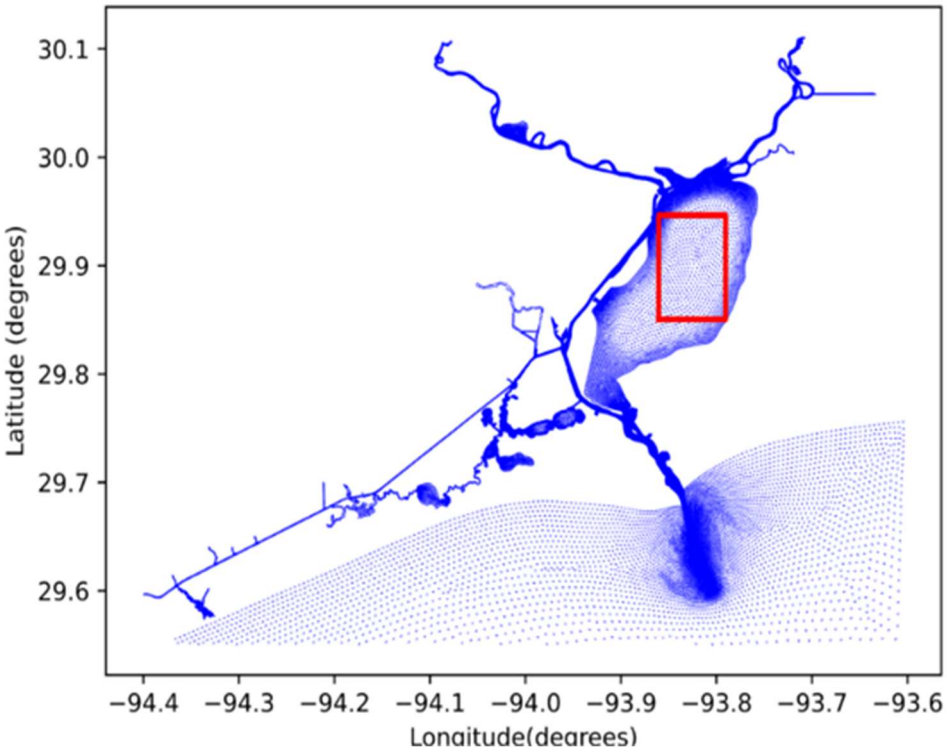

(**a**) SCHISM

Figure 11. *Cont.*

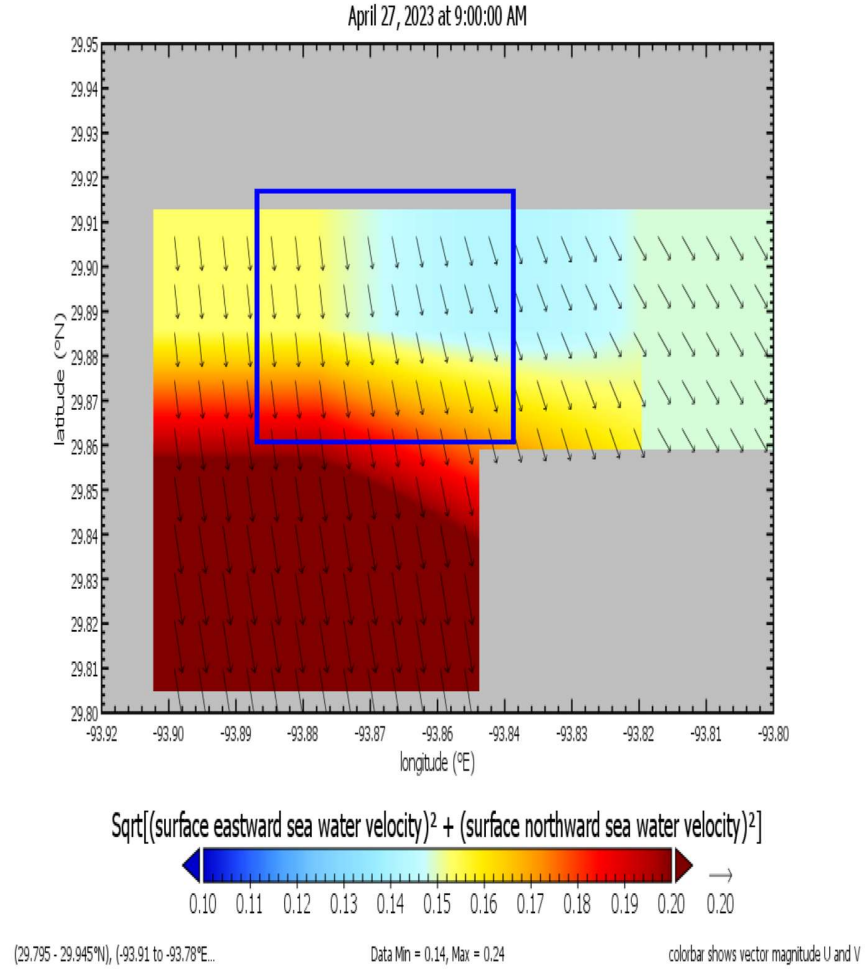

(**b**) HF radar

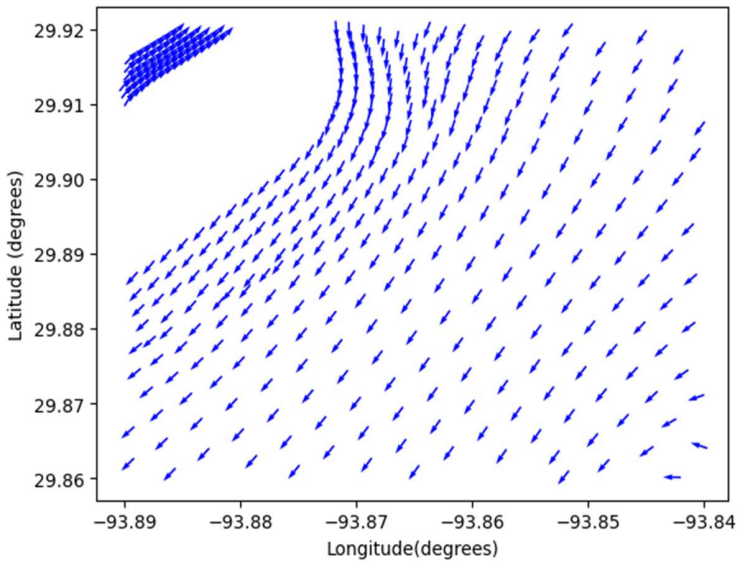

(**c**) A subplot from (**a**)

Figure 11. Plot of total current vectors produced by (**a**) SCHISM and (**b**) HF radar in SL (whole lake) at 9 a.m., 27 April 2023—color scale represents current speed in m/s. (**c**) A subplot (from a portion of the lake denoted by the red rectangle in (**a**)) of Total Current Vectors Derived from SCHISM in Sabine Lake, 27 April 2023 at 9 a.m.

3.4.2. Quantitative Analysis on 27 April at SL

Figures 12 and 13 reveal very remarkable insights into the performance of both the HF radar and SCHISM in generating the surface currents in the lake. Specifically, Figure 13 depicts the noteworthy very significant correlation coefficient of 0.95 for the magnitude of surface currents produced by the two methodologies on 27 April in Sabine Lake, Texas. This quantitative observation agrees with the observation of the dominant northward currents in the qualitative analysis in Figure 11.

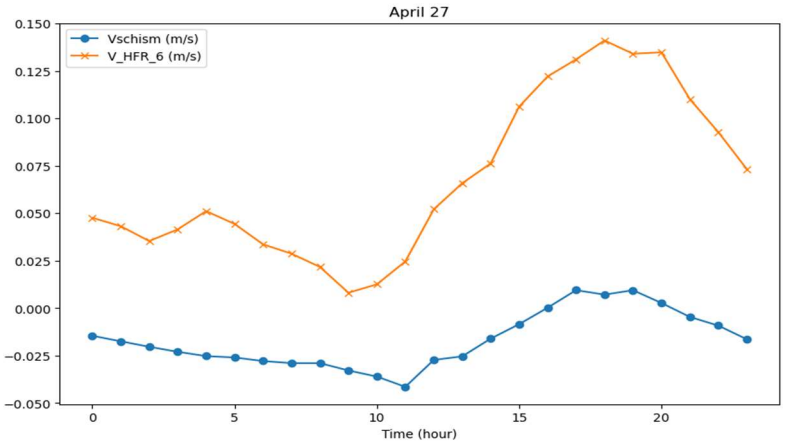

Figure 12. Comparison of northward currents from SCHISM (Vschism) and HF radar (V_HFR_6) over time at SL 27 April 2023.

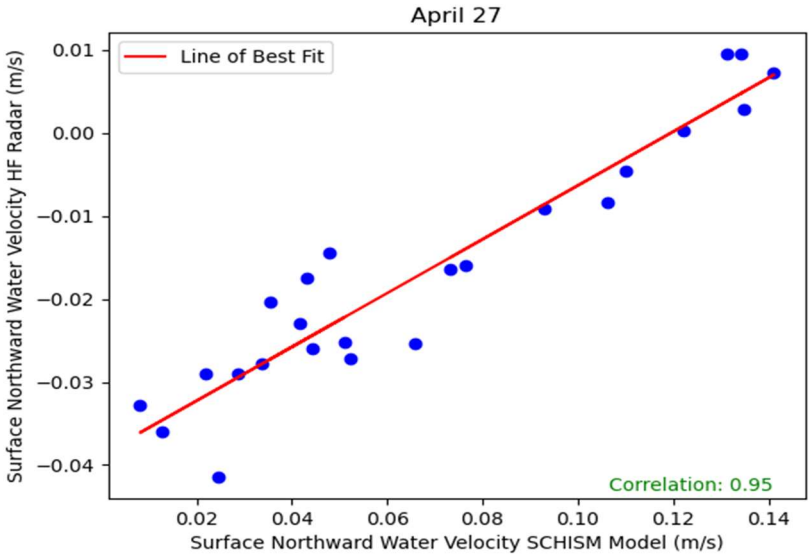

Figure 13. Correlation between the simulated (SCHISM) and observed (HF radar) hourly averages of northward currents (total water velocity) at SL for entire 24 h of 27 April 2023.

Figure 12 shows that in the first 12 h of the day, the model underestimated the speed of the currents by over 0.15 m/s, and even showed the currents to be in the opposite direction for the first 12 h of the day. However, the model represented the trend with the observation over 24 h well despite underestimating the speed of the current. The low value recorded by the model is due to the low conductivity arising from the low salinity that usually characterizes SL. The low salinity which is common in Sabine Lake (SL) is due to the freshwater inflows. Salinity influences the conductivity of the water—the more salt present in the water, the more its conductivity—and SCHISM incorporates salinity as its key input. Thus, low salinity (low ions) impacts the model water properties (such as conductivity)

and circulation dynamics. Lower salinity leads to lower water density which can influence the current patterns and flow rates, eventually influencing the model's predictions.

However, the model represented the trend with the observation over 24 h well despite underestimating the speed of the current. This could be also seen from the additional metrics adopted to evaluate the model on this day. The RMSE and MAE values for the currents measured by using the two methods on this day at the lake were estimated to be 0.09 and 0.08, respectively. The model was 47% in agreement with the radar in estimating the currents according to the IA estimate.

Tables 4 and 5 summarize the performance statistics of SCHISM in generating the surface currents in the study areas for the whole month of April 2023. The output of the simulation for 1 to 5 April was excluded from the intercomparison as these days were considered as a spin-up simulation period needed to establish a fully developed circulation. Both tables contain days when there was no distinct dominant direction of currents as well as other days that had similar outcomes described previously; both east and northward currents dominated, only northward currents dominated, and only eastward currents dominated. Table 4 shows that there were six (6) days (8, 9, 12, 16, 19, and 25 April) when both eastward and northward currents dominated the bay, nine (9) days (10, 11, 15, 17, and 26–30 April) when mostly northward currents dominated the bay and five (5) days (6, 7, 18, 21, and 24 April) when mostly eastward currents dominated the bay. In addition, there were five more days when no dominant component of currents persisted in the bay (13, 14, 20, 22, and 23 April). Similarly, in Table 5, there were two (2) days (21 and 25 April), when both eastward and northward currents dominated the lake, five (5) days (14, 18, 24, 27, and 30 April) when mostly a northward current dominated the lake, three (3) days (13, 26, and 28 April) when mostly an eastward current dominated the lake. There was a total of 11 days when no dominant component of currents persisted in the lake (7–10, 12, 15, 16, 17, 19, 23, and 29 April).

4. Discussion

Table 4 (above) provides a concise overview of the HF radar and SCHISM performance including days when the correlation coefficient of currents measured by both methods was significant ($corr \geq 0.5$). Figures 14–17 add more visualizations to understand the statistics used to evaluate the performance of the two methods.

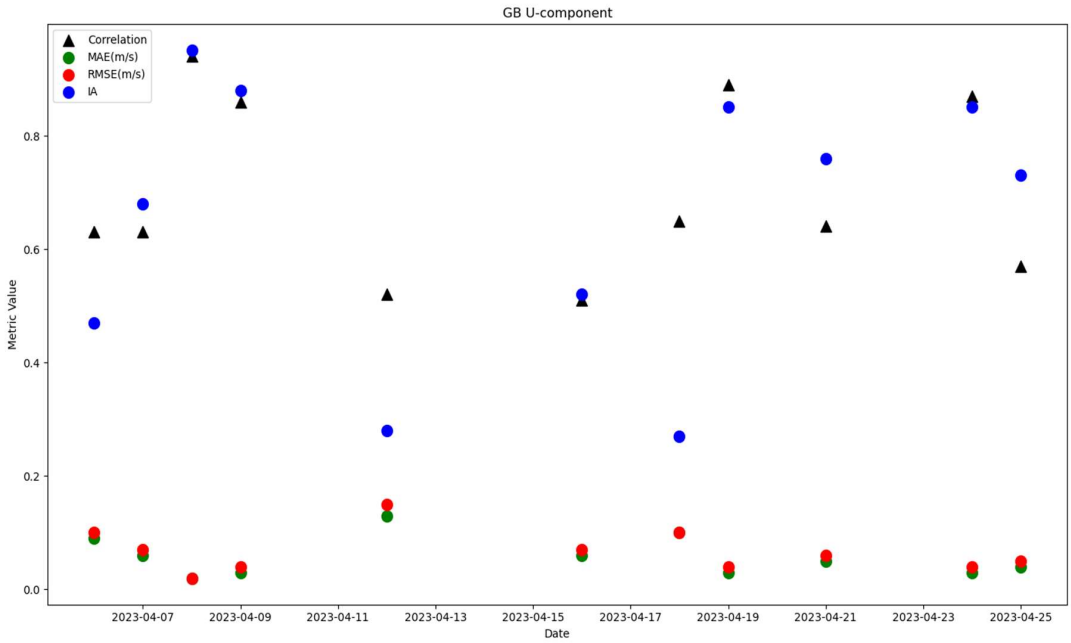

Figure 14. Plot of statistical evaluation of radar and model performance in predicting U-component current velocities at GB on days with significant correlation coefficients ($corr \geq 0.5$) only for the whole month of April 2023.

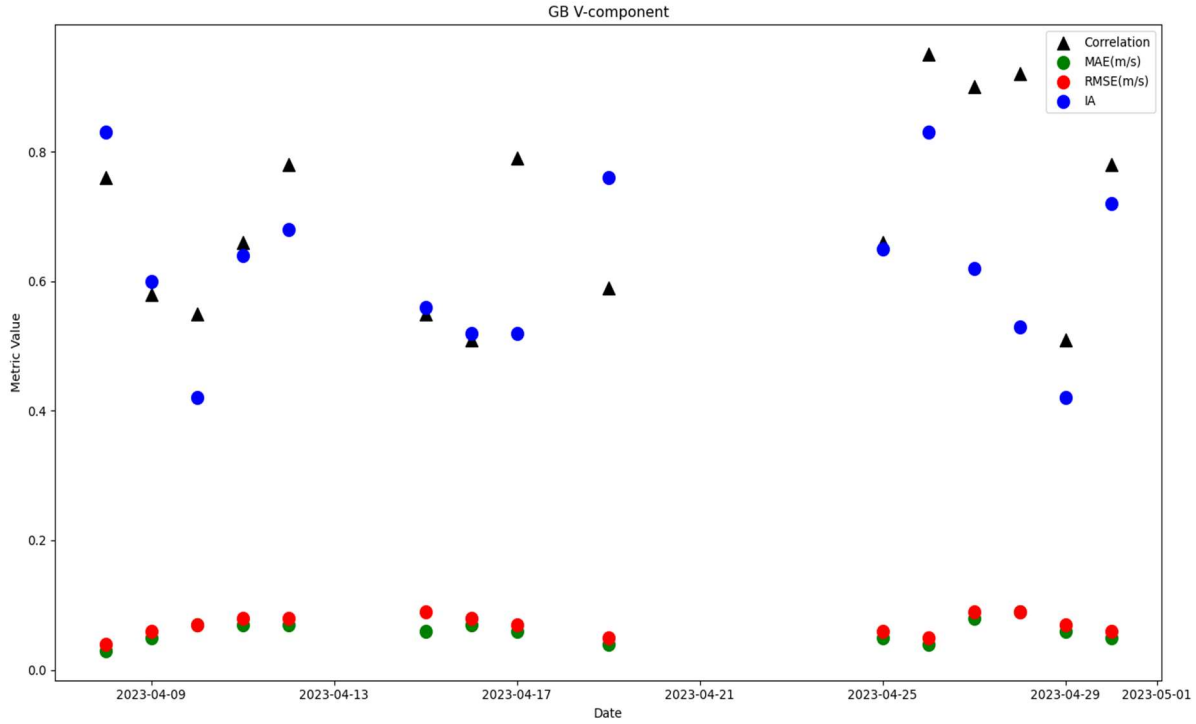

Figure 15. Plot of statistical evaluation of radar and model performance in predicting V-component current velocities at GB on days with significant correlation coefficients ($corr \geq 0.5$) only, whole month of April 2023.

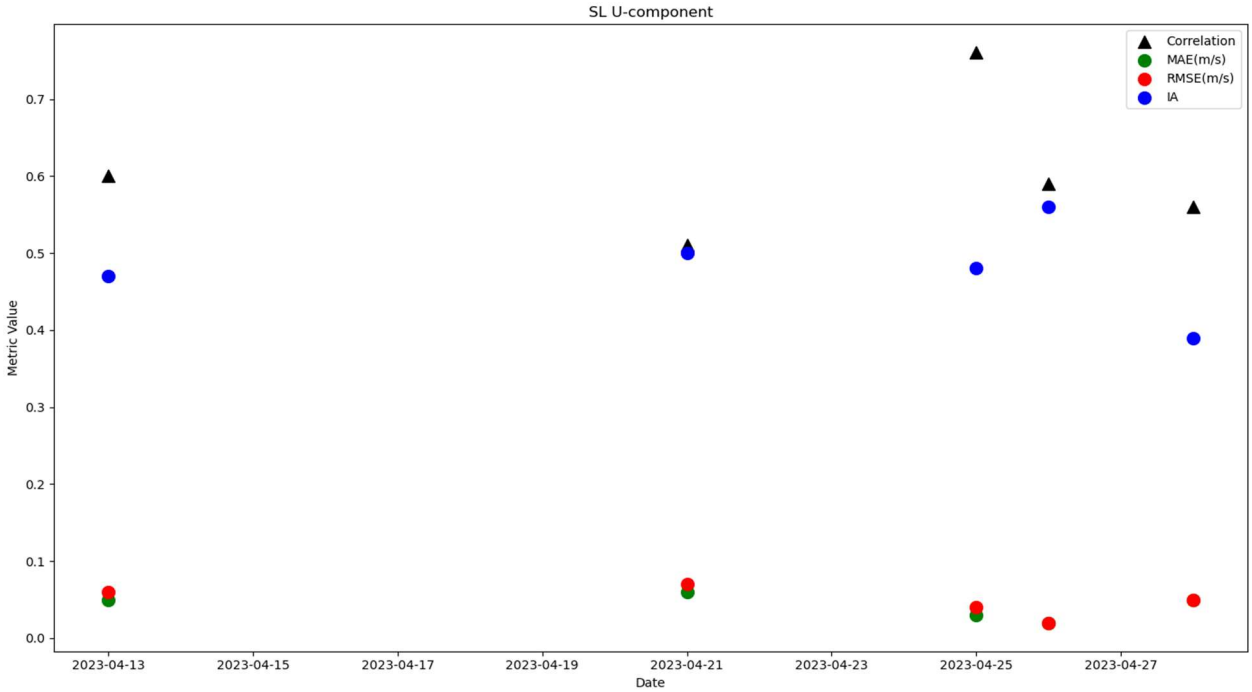

Figure 16. Plot of statistical evaluation of radar and model performance in predicting U-component current velocities at SL on days with significant correlation coefficients ($corr \geq 0.5$) only, whole month of April 2023.

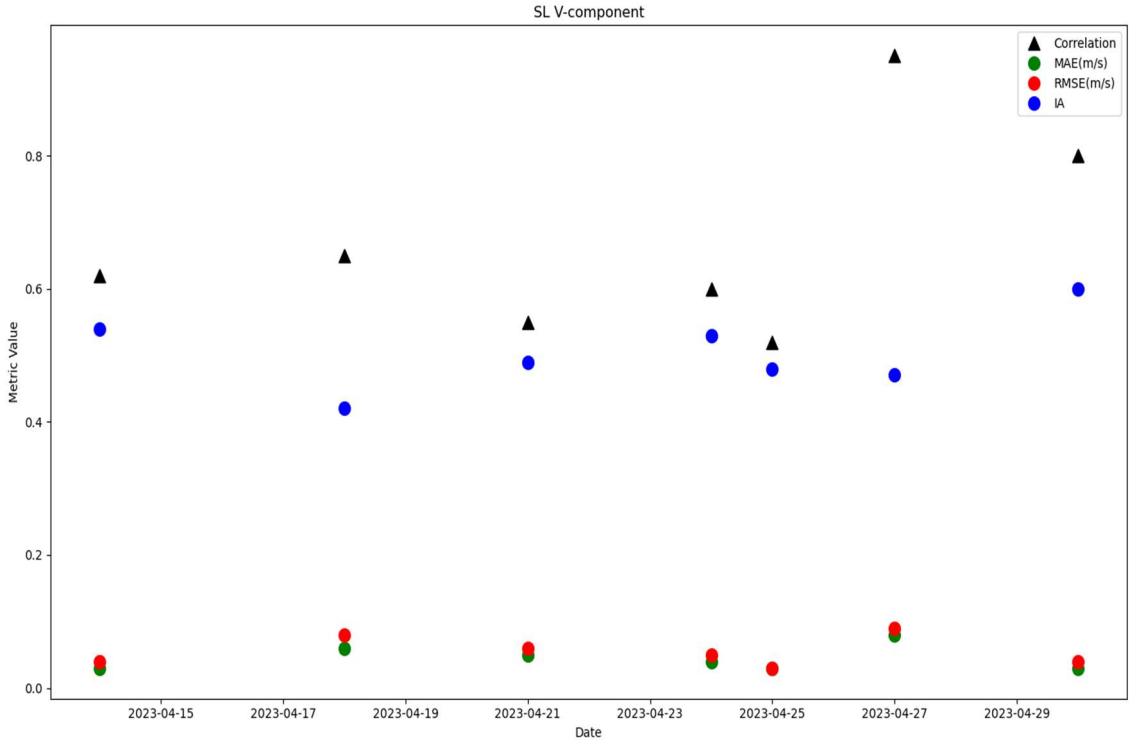

Figure 17. Plot of statistical evaluation of radar and model performance in predicting V-component current velocities at SL on days with significant correlation coefficients ($corr \geq 0.5$) only, whole month of April 2023.

In terms of the U-component on 8 April shown in Section 3.1.2 above, both the model and radar exhibited a strong correlation (corr.) of 0.94, indicating a high level of agreement in predicting eastward water velocities. The RMSE, MAE, and IA values further support the efficacy of the methods, with small error values in these metrics suggesting accurate predictions (Figure 14). On the other hand, 6 April exhibited a lower correlation (0.63) in the U-component, indicating a relatively weaker agreement between the model and radar predictions (in Figures 10 and 14). The associated error metrics for this date were higher, implying some discrepancy in predicting the eastward water velocities.

In general, the model predicted the U-component of the currents with high correlation values (low error values) at the beginning of the month and towards the end of the month with respect to days when the $corr \geq 0.5$ and had the least *corr* values in the middle of the months. This observation suggests the model's efficacy in capturing the physical processes driving the east–west (U) component of the currents at these times, and potentially stable forcing conditions such as tidal cycles and wind patterns, which are represented well by the model at the start and end of the month. At the middle of the month, the relatively lower *corr* values and higher RMSE and MAE values could indicate the presence of more complex or rapidly changing conditions like storms or nonlinear interactions which were not fully captured by the model.

On 27 April 2023 (see Section 3.2 above), in the bay, both methods captured effectively the northward water movement (Figure 15). The V-component correlation coefficient was substantial at 0.9, suggesting the reliability of the two methods in measuring the surface currents on this day. Generally, Figure 15 indicates that there was a more dominant northward current in the bay, especially towards the end of the month, i.e., 26–28, and 30 April with *corr* values of approximately 0.8 or more. It can also be observed from Figure 15 that the error values (MAE and RMSE) for days with a *corr* value ≥ 0.5 for the V-component of the current maintained a similar trend with the RMSE, always slightly higher than the MAE.

The observed minor disparity in the precise measurements of the currents by using the two methodologies in the eastward and northward directions could be attributed to a combination of factors including the wind dynamics within the bay, seasonal weather patterns prevalent in the month of April in the bay, and influence of the bay's proximity to the Gulf of Mexico. Park [29] observed that the dominant winds in the bay are the southeasterly winds, and the bay–ocean interactions are usually influenced through the north-eastern direction. Salas-Monreal [1] inferred from his work that southerly winds dominate the bay from October to April, while northerly winds are more pronounced in the bay from May to September. Thus, the month of April is usually characterized by variable wind patterns in the bay, primarily driven by prevailing winds from the east or southeast. These findings support the outcomes summarized as shown in Figures 14 and 16 (as well as shown in Figures 3, 4, 9, and 10) for 8 April and 6 April, respectively. Moreover, the anticipated shift towards northerly winds dominating the bay by the end of April aligns with the result, which showed that the model estimated more northward currents precisely, reflected in a correlation coefficient of 0.8 or more, summarized in Figure 15 (as well as in Table 4).

From Table 5, we can see the summary of the comparison between the values of the currents estimated by the model and the radar, including days when the *corr* values were significant ($corr \geq 0.5$) in Sabine Lake. It can be observed from Table 5 that there were very few days when the currents estimated by the model had a significant correlation coefficient. There were only five (5) days when the east–west (U-component) current dominated the lake as observed in Figure 16 and Table 5 above. In terms of the V-component of the current velocity (Figures 13 and 17) and the result presented in Section 3.4.2, the significant correlation coefficient of 0.95 indicates that there was similar agreement in predicting the northward water velocities on 27 April in the lake by using both methods. This result shows the model's effectiveness in capturing the overall northward current pattern and key hydrodynamic processes within the lake on that day as well as on other days when a north–south (V-component) current dominated the lake. However, despite the strong correlation, the high error values (RMSE and MAE) for this day (Table 5, Figure 17) point to the discrepancies in the magnitude of the currents measured by the model and radar. While the model effectively mirrors the trends, there were differences between the simulated and measured currents, especially the finer details of the current velocities earlier described in Section 3.4.2. Willmott's index of agreement value of 47% (0.47) also points to this deviation in the measurement.

Overall, the observations from Table 5 and Figures 16 and 17 indicate that only a few days showed a significant correlation between the model's estimated currents and observed values in SL. The lake's low and variable salinity, attributed to its low salt content [30] could have played a prevalent role in influencing the radar's ability to estimate the surface currents in the lake. The HF radar system relies on Bragg's scattering, and in low conductivity places, like SL, the absence of sufficient salinity reduces the radar's ability to produce strong Bragg's scattering, making it difficult for it to detect the current vectors on many days. This was the case on 6, 11, 20, and 23 April (Table 5), when it was difficult for the radar to produce any vectors, and hence no good quality data to make any intercomparisons. There were other days when Bragg's scattering was very weak to produce enough vectors and thus poor-quality data resulted. These contributed to the lack of significant correlation between the model's estimations and actual observations on many days at SL. Thus, the poor correlation observed in SL may not reflect the model's deficiencies in estimating the currents in the area but rather the environmental limitations of using HF radar in such settings.

4.1. Physical Processes Affecting the Model and Radar Agreement

Possible physical processes that influenced the results of the comparisons between the HF radar and SCHISM simulations include wind forcing, tidal dynamics, and freshwater inflow.

4.1.1. Wind Forcing

Shallow coastal regions like Galveston Bay and Sabine Lake, Texas, have wind-driven currents which can be highly variable. During the month of April, the wind patterns in the Gulf of Mexico change quite abruptly, usually influenced by seasonal shifts typical of the transition from the colder winter to warmer spring. The North American Mesoscale forecast system (NAM) 6-hourly reanalysis data were utilized to calculate the wind stress at each model grid. While the NAM 6-hourly reanalysis data are effective at capturing large-scale, synoptic wind patterns and providing robust wind forcing for SCHISM, its temporal and spatial limitations (the 6-hourly interval in NAM wind data can cause temporal smoothing of wind-driven events like sea breezes, cold fronts or storms, and gusts known to occur in the region during the onset of spring which could lead to current mismatches or reversal) can lead to smoothing of high-frequency wind variability.

HF radar, which measures surface currents directly, is highly responsive to short-term wind variability making it more sensitive to transient wind-driven events. Particularly, while both datasets show similar trends in the current direction (Figures 3a,b, 6, and 9) and timing (Figure 3), the model tends to smooth out the short-term variations that the radar detects more clearly. Since SCHISM is forced by 6 h NAM wind data, it may not capture high-frequency wind variability (gusts, sea breezes) that the radar is more responsive to.

Based on the general weather patterns, the whole of the Texas coast experiences cold fronts, sea breezes, and occasional thunderstorms during this time of the year [31,32]. April is usually a transition period from colder winter weather to warmer summer conditions, so cold fronts and gusty winds could have passed through the area (Texas coast, and by extension, Galveston Bay and Sabine Lake). Local sea breezes, driven by the land heating up faster than the water, are common along the coast and result in daily wind shifts as cooler air moves from the sea towards the land which is warmer.

4.1.2. Tidal Dynamics

In Galveston Bay and Sabine Lake, tidal currents drive most of the surface circulation. Usually, the semi-diurnal tides—two high and two low tides per day which create oscillating currents—are the dominant drivers of the surface circulation in this region as highlighted previously by [33,34]. In the SCHISM set up, the tidal offshore boundary was forced by the observed NOAA tide station data from the Galveston Bay entrance (NOAA 8771341) and Sabine Pass (NOAA 8770822) capturing the influence of semi-diurnal tides. The overall impact of considering this tidal influence is that SCHISM, which is well suited to represent the tidal dynamics, tends to show good agreement with the radar data in regions and times when tidal currents dominate. However, differences between the SCHISM and HF radar data may arise due to short-term, high-frequency events such as wind gusts or local wind forcings, which the HF radar captures more accurately because of its continuous monitoring of the real-time surface currents.

From the tidal data above in Figures 18 and 19 representing the Galveston Bay entrance (GB) and Texas Point, Sabine Pass (SL), the semi-diurnal tidal pattern (two high and two low tides per day) dominated the bay and lake throughout the entire month in April 2023 with notable high tidal ranges on 10–13 April and 24 April in GB (Figure 19, Table 6). These tides significantly influence the surface current patterns, especially in shallow estuaries such as GB and SL, and SCHISM's tidal forcing simulates these oscillations well, especially during the higher tidal range.

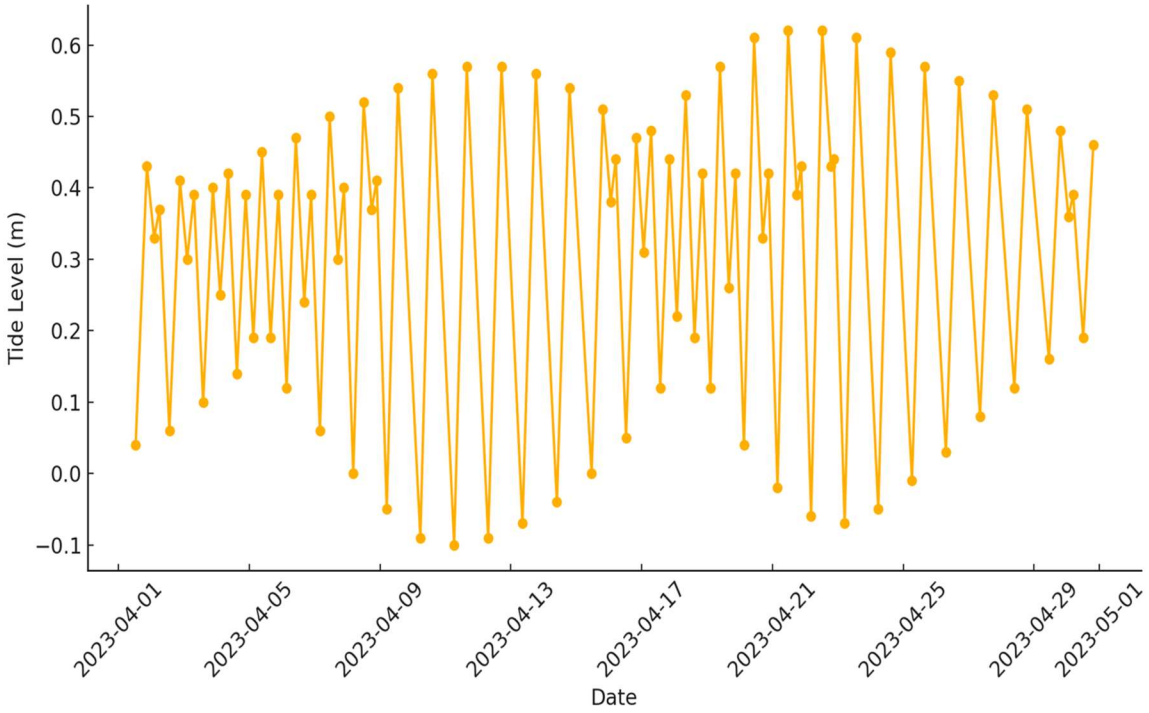

Figure 18. Tide predictions for April 2023 derived from data at NOAA tidal station at the Galveston Bay entrance, North Jetty (Station ID: 8771341).

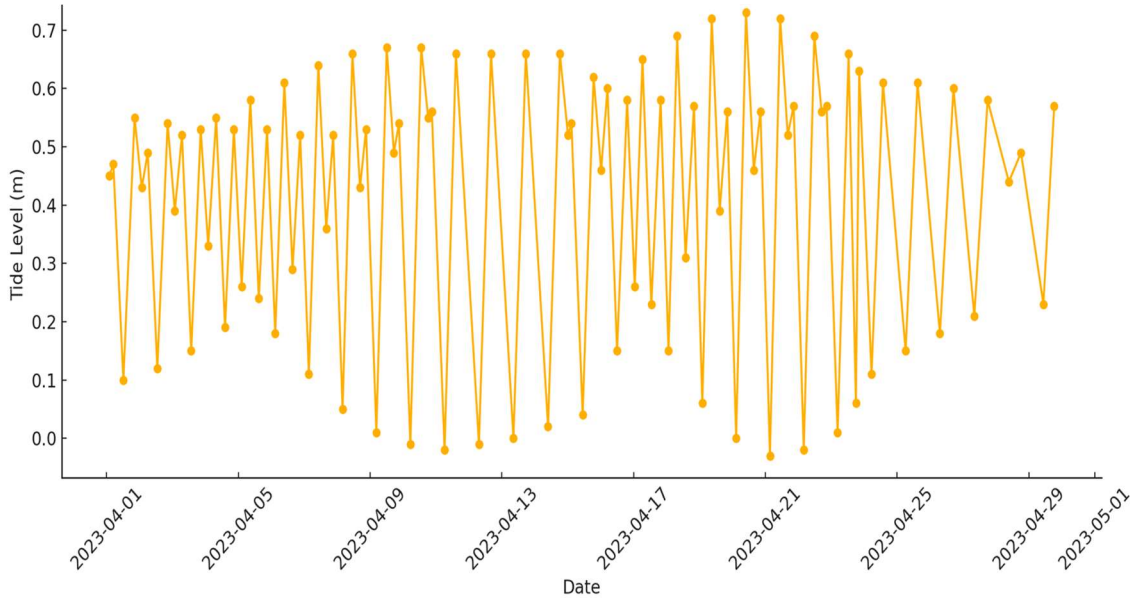

Figure 19. Tide predictions for April 2023 derived from data at NOAA tidal station at Texas Point, Sabine Pass, TX (Station ID: 8770822).

The statistical evaluation metrics (correlation, RMSE, MAE, IA) in Figures 14 and 15 highlight the periods of stronger and weaker agreement between the model and radar. It could be observed that periods with high correlation values, such as around 8 April in GB, coincide with stronger tidal currents (Figure 18) suggesting that the model performs well in capturing large-scale tidal dynamics while periods with lower correlation values, such as around 17 April, may be attributed to local wind variability, local non-tidal factors, or other environmental factors. Similarly, in SL, the high tides tend to cause a stronger inflow of water from the Gulf of Mexico through the Sabine Pass while low tide periods

possibly correspond to a high outflow from SL. Depending on the source, the influx of water into the lake can strengthen the surface current—more saline water from the Gulf of Mexico—leading to more dynamic variations captured well by the model. This could result in the high correlation values observed on 25 April in the U–component (Figure 16) and 27 April in the V-component (Figure 17). Conversely, we observed a low correlation around 10–12 April which corresponds to the low tide periods (Figures 16, 17 and 19; Table 5). These low tides may cause a weaker current flow due to the less dynamic water movement and the model's performance may show slight variations in accuracy (poor performance) as a result.

Table 6. Overview of tidal range for April 2023 at Galveston Bay entrance, North Jetty State: TX (Station ID: 8771341).

Date	Low Tide (m)	High Tide (m)	Tidal Range (m)
1 April 2023	0.04	0.43	0.39
2 April 2023	0.06	0.41	0.35
3 April 2023	0.1	0.4	0.3
4 April 2023	0.14	0.42	0.28
5 April 2023	0.19	0.45	0.26
6 April 2023	0.24	0.47	0.23
7 April 2023	0.3	0.5	0.2
8 April 2023	0.37	0.52	0.15
9 April 2023	0.54	0.41	−0.13
10 April 2023	−0.09	0.56	0.65
11 April 2023	−0.1	0.57	0.67
12 April 2023	−0.09	0.57	0.66
13 April 2023	−0.07	0.56	0.63
14 April 2023	−0.04	0.54	0.58
15 April 2023	0	0.51	0.51
16 April 2023	0.05	0.47	0.42
17 April 2023	0.12	0.48	0.36
18 April 2023	0.19	0.53	0.34
19 April 2023	0.26	0.57	0.31
20 April 2023	0.33	0.61	0.28
21 April 2023	0.39	0.62	0.23
22 April 2023	0.43	0.62	0.19
23 April 2023	0.61	0.44	−0.17
24 April 2023	−0.05	0.59	0.64
25 April 2023	−0.01	0.57	0.58
26 April 2023	0.03	0.55	0.52
27 April 2023	0.08	0.53	0.45
28 April 2023	0.12	0.51	0.39
29 April 2023	0.16	0.48	0.32
30 April 2023	0.19	0.46	0.27

In addition to the wind and tidal dynamics, the model and radar performance may also be influenced by freshwater inflows, particularly in regions like Sabine Lake, where riverine inputs affect the salinity and current patterns. Quantitative data on freshwater inflows from USGS stations were incorporated into SCHISM with a notable contribution from Cedar Lakes (see Figure 1).

4.2. Possible Limitations

Our results above are not insensitive to the possible measurement errors and signal-to-noise ratio issues associated with HF radar data and limitation in model resolution parametrization issues associated with models like SCHISM. These could have been the possible causes of some of the observed discrepancies in the direction of the simulated and measured currents observed, most especially in the cases of very weak currents. Measurement errors which are inherent in any observational system affect HF radars due

to the complex nature of electromagnetic wave interactions with the ocean surface, which can affect the accuracy of current velocity measurements. Furthermore, the spatial and temporal variability of ocean surface currents can introduce uncertainties, especially when the currents are weak or highly turbulent, leading to discrepancies between the observed and simulated currents, explaining the probable cause why the direction of the measured currents was opposite to the simulated one on a few occasions.

Similarly, the signal-to-noise ratio in the HF radar data can significantly impact the quality of HF radar measurement, especially when measuring low current speeds. A low signal-to-noise ratio means that the true current velocity (true signal) is difficult to distinguish from background noise, leading to less reliable data and misinterpretation of the current magnitudes and directions. Another important factor to consider is that numerical models like SCHISM rely on many assumptions and parametrization to simulate complex oceanographic processes in coastal estuarine environments. If the model does not accurately capture the small-scale processes, especially on the surface like the HF radar, or the parametrizations do not accurately represent the physical processes in the coastal estuarine environment, the model output may deviate from the actual (observational) measurements.

A combination of these factors might have contributed to isolated observed cases where the measured current direction was opposite to the simulated one, most especially in the cases of very weak currents, where such discrepancies are likely to occur.

5. Conclusions

This study has shed more light on the intricate dynamics of the surface current measurements within Galveston Bay and Sabine Lake, as exhibited during the month of April 2023. The good correlation between the model's (SCHISM) predicted currents with HF radar measured currents during the observational periods when the environmental conditions were conducive to HF radar measurements (such as adequate surface conductivity, proper ocean wave conditions, i.e., Bragg's wavelength) is indicative of the model's capacity to predict surface currents.

The observed less precise or moderately correlated measurements of surface currents by using both methods on some days, especially in Sabine Lake, are attributed to environmental factors such as wind dynamics, salinity, and seasonal weather patterns.

We believe that the observed differences in measurements of eastward and northward directions across different dates presented above highlight the complex relationship between the prevailing winds, interactions between the bay and ocean, and regional weather patterns. Our assertion above hinges on the previous works of [1,30] which provided insight into how wind patterns affect the surface current behavior in Galveston Bay.

Regarding the qualitative comparison and its relationship to the result of the quantitative analysis, it was observed that days characterized by predominant northward currents exhibited significant correlation coefficients exclusively in the northward direction in the bay and lake. Similarly, on days dominated by eastward currents, the correlation coefficients for currents measured by both the model and HF radar were significant only in the eastward direction for the bay. Notably, SCHISM and HF radar also effectively captured the trend and magnitude of surface currents on days with both eastward and northward currents in the bay. This is an important finding from this study.

This research finding emphasizes the importance of considering the environmental variables in surface current predictions using hydrodynamic models like SCHISM and HF radar, especially in regions influenced by coastal dynamics like Galveston Bay and Sabine Lake. SCHISM exhibited comparable performance in accurately simulating the surface currents, aligning closely with the established methodology of HF radar. This suggests the potential extension of SCHISM's applicability to study various environmental phenomena such as coastal flooding and storm surges along the Texas coast. Very importantly, this study contributes valuable insights into the intricate relationship between the wind dynamics and surface current behavior, advancing our understanding of the coastal dynamics and providing strategies for environmental monitoring and management.

The data used for this study are unique to the Texas coast and specific to Galveston Bay and Sabine Lake. It is our belief that the methodologies established, and modeling techniques described in this study may be applicable to the intercomparison of the surface currents produced by High-Frequency radar and SCHISM at other estuaries along the Texas coast or elsewhere if similar data can be sourced there.

Author Contributions: Conceptualization, C.O.O. and R.M.F.; methodology, C.O.O., R.M.F. and J.L.; formal analysis, C.O.O. and R.M.F.; software C.O.O., R.P. and J.P.-G.; resources, C.F., R.P., J.P.-G. and J.L.; visualization, C.O.O. and J.P.-G.; writing—original draft preparation, C.O.O.; writing—review and editing, R.M.F., J.L. and C.F.; supervision, R.M.F.; project administration, R.M.F. and C.F.; funding acquisition, R.M.F. and C.F. All authors have read and agreed to the published version of the manuscript.

Funding: This research was made possible by the GLO CMP-26 Project of Special Merit: HF RADARS FOR TEXAS BAYS AND PORTS with award number (Glo Contract No.) 21-155-002-C874. Some authors were supported by the NOAA Center for Atmospheric Science—Meteorology (NCASM II), which is funded by the U.S. Department of Commerce, National Oceanic and Atmospheric Administration, Educational Partnership Program under Agreement No. NA22SEC4810015.

Institutional Review Board Statement: Not applicable.

Informed Consent Statement: Not applicable.

Data Availability Statement: Data sources used in this research are all contained within the article.

Acknowledgments: The authors would like to acknowledge Hector Aguilar from CODAR Ocean Sensors for his invaluable help retrieving the HF radar data and technical support.

Conflicts of Interest: Author Christopher Fuller was employed by Research, Applied Technology Education Services, Inc. The remaining authors declare that the research was conducted in the absence of any commercial or financial relationships that could be construed as a potential conflict of interest.

References

1. Salas-Monreal, D.; Anis, A.; Salas-de-Leon, D.A. Galveston Bay dynamics under different wind conditions. *Oceanologia* **2018**, *60*, 232–243. [CrossRef]
2. Qian, Q.; Su, L.; Zaloom, V.; Jao, M.; Wu, X.; Wang, K.-H. Field Measurements and Modelling of Vessel-Generated Waves and Caused Bank Erosion—A Case Study at the Sabine-Neches Waterway, Texas, USA. *Water* **2023**, *15*, 35. [CrossRef]
3. Röhrs, J.; Sutherland, G.; Jeans, G.; Bedington, M.; Sperrevik, A.K.; Dagestad, K.-F.; LaCasce, J.H. Surface currents in operational oceanography: Key applications, mechanisms, and methods. *J. Oper. Oceanogr.* **2021**, *16*, 60–88. [CrossRef]
4. Mantovani, C.; Corgnati, L.; Horstmann, J.; Rubio, A.; Reyes, E.; Quentin, C.; Cosoli, S.; Asensio, J.L.; Mader, J.; Griffa, A. Best Practices on High-Frequency Radar Deployment and Operation for Ocean Current Measurement. *Front. Mar. Sci.* **2020**, *7*, 210. [CrossRef]
5. Chiu, C.; Huang, C.; Wu, L.; Zhang, Y.; Chuang, L.; Fan, Y.; Yu, H.-C. Forecasting of Oil Spill Trajectories by using SCHISM and X-band radar. *Mar. Pollut. Bull.* **2018**, *137*, 566–581. [CrossRef]
6. Saviano, S.; Kalampokis, A.; Zambianchi, E.; Uttieri, E. A year-long assessment of wave measurements retrieved from an HF adar network in the Gulf of Naples (Tyrrhenian Sea, Western Mediterranean Sea). *J. Oper. Oceanogr.* **2019**, *12*, 1–15. [CrossRef]
7. Barth, A.; Alvera-Azcárate, A.; Weisberg, R.H. Assimilation of high-frequency radar currents in a nested model of the West Florida Shelf. *J. Geophys. Res.* **2008**, *113*, C08033. [CrossRef]
8. Paduan, J.D.; Shulman, I. HF Radar data assimilation in the Monterey Bay area. *J. Geophys. Res.* **2004**, *109*, C07S09. [CrossRef]
9. Crombie, D.D. Doppler spectrum of sea echo at 13.56 Mc/s. *Nature* **1955**, *175*, 681–682. [CrossRef]
10. Laws, K. Measurement of Near Surface Ocean Currents Using HF Radar. Ph.D. Thesis, University of California, Santa Cruz, CA, USA, 2005.
11. Morales-Marquez, V.; Dumas, D.; Guerin, C.A. HF Radar estimation of ocean wave parameters: Second-order Doppler spectrum versus Bragg wave modulation approach. *arXiv* **2024**, arXiv:2407.07658. [CrossRef]
12. Kirby, J.T. Recent advances in nearshore wave, circulation, and sediment transport modeling. *J. Mar. Res.* **2017**, *75*, 263–300. [CrossRef]
13. Kalampokis, A.; Uttieri, M.; Poulain, P.-M.; Zambianchi, E. Validation of HF Radar-Derived Currents in the Gulf of Naples with Lagrangian Data. *IEEE Geosci. Remote Sens. Lett.* **2016**, *13*, 1452–1456. [CrossRef]
14. Ohlmann, C.; White, P.; Washburn, L.; Terrill, E.; Emery, B.; Otero, M. Interpretation of coastal HF Radar–derived surface currents with high-resolution drifter data. *J. Atmos. Ocean. Technol.* **2007**, *24*, 666–680. [CrossRef]

15. Pitcher, C.R.; Lawton, P.; Ellis, N.; Smith, S.J.; Incze, L.S.; Wei, C.L.; Greenlaw, M.E.; Wolff, N.H.; Sameoto, J.A.; Snelgrove, P.V. Exploring the role of environmental variables in shaping patterns of seabed biodiversity composition in regional-scale ecosystems. *J. Appl. Ecol.* **2012**, *49*, 670–679. [CrossRef]
16. Azevedo, A.; Oliveira, A.; Fortunato, A.B.; Zhang, J.; Baptista, A.M. A cross-scale numerical modeling system for management support of oil spill accidents. *Mar. Pollut. Bull.* **2014**, *80*, 132–147. [CrossRef]
17. Zhang, Y.J.; Ye, F.; Stanev, E.V.; Grashorn, S. Seamless cross-scale modelling with SCHISM. *Ocean Model.* **2016**, *102*, 64–81. [CrossRef]
18. Li, D.; Wang, Z.; Xue, H.; Thomas, A.C.; Pettigrew, N.; Yund, P.O. Seasonal variations and driving factors of the Eastern Maine Coastal Current. *J. Geophys. Res. Ocean.* **2021**, *126*, e2021JC017665. [CrossRef]
19. Dye, B.; Jose, F.; Allahdadi, M.N. Circulation dynamics and seasonal variability for the Charlotte Harbor Estuary, Southwest Florida coast. *J. Coast. Res.* **2019**, *36*, 276–288. [CrossRef]
20. Allahdadi, M.N.; Jose, F.; D'Sa, E.J.; Ko, D.S. Effect of wind, river discharge, and outer-shelf phenomena on circulation dynamics of the Atchafalaya Bay and shelf. *Ocean Eng.* **2017**, *129*, 567–580. [CrossRef]
21. Willmott, C.J. On the validation of models. *Phys. Geogr.* **1981**, *2*, 184–194. [CrossRef]
22. Willmott, C.J.; Matsuura, K. Advantages of the Mean Absolute Error (MAE) over the Root Mean Square Error (RMSE) in Assessing Average Model Performance. *Clim. Res.* **2005**, *30*, 79–82. [CrossRef]
23. Dupuis, K.W.; Anis, A. Observations and modeling of wind waves in a Shallow Estuary: Galveston Bay, Texas. *J. Waterw. Port CASCE* **2013**, *139*, 314–325. [CrossRef]
24. Lee, J.; Jungwoo, L.; Sang-Leen, Y.; Seog-Ku, K. Three-Dimensional Unstructured Grid Finite-Volume Model for Coastal and Estuarine Circulation and Its Application. *Water* **2020**, *12*, 2752. [CrossRef]
25. Fuller, C.; Andrew, E.; Scoggins, M.; Haselbach, L.; Ogbodo, C.O.; Fitzgerald, R.; Wu, X. Long-Term Coastal Observatory-High Frequency Radar Commissioning Process and Considerations. *Discov. Water* 2024, *submitted*.
26. Cosoli, S.; Gacic, M.; Mazzoldi, A. Comparison between HF Radar current data and moored ADCP currentmeter. *Nuovo C* **2005**, *28C*, 865–879. [CrossRef]
27. Chapman, R.D.; Shay, L.K.; Graber, H.C.; Edson, J.B.; Karachintsev, A.; Trump, C.L.; Ross, D.B. On the accuracy of HF radar surface current measurements: Intercomparisons with ship-based sensors. *J. Geophys. Res. Ocean.* **1997**, *102*, 18737–18748. [CrossRef]
28. Du, J.; Park, K.; Shen, J.; Zhang, Y.J.; Yu, X.; Ye, F.; Rabalais, N.N. A hydrodynamic model for Galveston Bay and the shelf in the northern Gulf of Mexico. *Ocean Sci.* **2019**, *15*, 951–966. [CrossRef]
29. Park, J.S.; Wade, T.L.; Sweet, S. Atmospheric distribution of polycyclic aromatic hydrocarbons and deposition to Galveston Bay, Texas, USA. *Atmos. Environ.* **2001**, *35*, 3241–3249. [CrossRef]
30. Wang, H.; Zhang, N. Calibration Validation of Hydrodynamics Salinity Transport Model for Sabine Lake Water System. *J. Fluids Eng.* **2019**, *141*, 104502. [CrossRef]
31. Romero-Arteaga, A.; Alegria-Arzaburu, A.R.; Rivas, D.; Juarez, B. Nearshore current variations during the passage of cold fronts in NW Gulf of Mexico. *Cont. Shelf Res.* **2022**, *238*, 104697. [CrossRef]
32. Osteimeier, G. The Texas Sea breeze. Facts or fiction? An investigation of Texas Climate Records for a Sea-Land Breeze Signature. Ph.D. Thesis, Texas A&M University, College Station, TX, USA, 1998.
33. Xu, J.; Myers, E.P.; Jeong, I.; White, S.A. *VDatum for the Coastal Waters of Texas and Western Louisiana: Tidal DAtums and Topography of the Sea Surface, NOAA Technical Memorandum*; NOS CS 29; NOAA: Silver Spring, MD, USA, 2013. Available online: https://repository.library.noaa.gov/view/noaa/2640 (accessed on 14 October 2024).
34. Huang, W.; Zhang, Y.J.; Wang, Z.; Ye, F.; Moghimi, S.; Myers, E.; Yu, H. Tidal simulation revisited. *Ocean Dyn.* **2022**, *72*, 187–205. [CrossRef]